DTU

DTU Library

Definition of the IEA Wind 22-Megawatt Offshore Reference Wind Turbine

Zahle, Frederik; Barlas, Athanasios; Lønbæk, Kenneth; Bortolotti, Pietro; Zalkind, Daniel; Wang, Lu ; Labuschagne, Casper ; Sethuraman, Latha; Barter, Garrett

April 2024

IEA Wind TCP Task 55

Definition of the IEA Wind 22-Megawatt Offshore Reference Wind Turbine

Technical Report

iea wind

Definition of the IEA Wind 22-Megawatt Offshore Reference Wind Turbine

Frederik Zahle[1]
Thanasis Barlas[1]
Kenneth Lønbæk[1]
Pietro Bortolotti[2]
Daniel Zalkind[2]
Lu Wang[2]
Casper Labuschagne[2]
Latha Sethuraman[2]
Garrett Barter[2]

[1]Technical University of Denmark
[2]National Renewable Energy Laboratory

Document information

Contents

1 Introduction

1.1 Importance of Reference Wind Turbines

Reference wind turbines (RWTs) serve an important purpose in the wind energy community because they provide openly available data for models representative of current wind turbine technology. Practitioners use these models across a range of fidelities for a variety of purposes, from aerodynamic, structural, and aeroelastic turbine modeling to wind farm flow modeling. Early examples of RWTs were the National Renewable Energy Laboratory (NREL) Wind Partnership for Advanced Component Technology (WindPACT) turbine series [1], followed by the popular NREL 5 MW RWT [2] and the Technical University of Denmark (DTU) 10 MW RWT [3]. The effort to develop and maintain RWTs was strengthened and formalized within the International Energy Agency Wind Technology Collaboration Programme (IEA Wind) Task 37 "Wind Energy Systems Engineering: Integrated Research, Design, Development, and Operation" [4], within which three new RWTs were defined, namely, the IEA 3.4 MW, IEA 10 MW, and IEA 15 MW RWTs [5, 6]. The usefulness and popularity of these RWTs are proven by the hundreds of citations of technical reports describing the various models and by the dozens of forks (copies) of their GitHub repositories.

During IEA Wind Task 37, an ontology named WindIO was also developed to describe wind turbines and wind power plants [7]. The ontology was used for the last three RWTs at 3.4, 10, and 15 MW. Given the continued development of commercial turbine technology and upscaling of machines to larger power ratings, the definition of new RWTs and the maintenance of those in operation remain priorities for the wind energy community [8]. In light of this, a continuation of IEA Wind Task 37 was established: IEA Wind Task 55 REFWIND – Reference Wind Turbines and Plants [9]. Task 55 focuses on developing and maintaining reference systems and continues the development of the WindIO ontology.

1.2 Need for a Larger Offshore Reference Wind Turbine

The offshore wind energy market has been dominated by a continuous upscaling of turbine power rating and rotor size during the last decade. At the time of writing, the largest installed offshore turbine prototypes have power ratings between 14 and 16 MW, although announcements have already been made about future prototypes surpassing 20 MW. It remains an open question whether the current trend of upscaling will continue or whether the size of commercially installed turbines will reach a plateau. Therefore, it is important that the wind energy community has access to realistic and common reference systems to investigate future turbine technology—not only to identify the technological challenges of such large machines but also to investigate whether numerical modeling tools and design practices require further development to be suitable for the next generation of machines. A user survey sent to Tasks 37 and 55 participants and stakeholders indicated the need for an offshore RWT with a power rating of 22 MW to model machines with projected installation in the 2025–2030 time frame. The target became a Class 1-B machine with a rotor specific power nearing $350\ \mathrm{W\,m^{-2}}$. The survey also recommended designing for an increased maximum blade tip speed of $105\ \mathrm{m\,s^{-1}}$ and to design both a fixed-bottom offshore foundation and a semisubmersible floating platform. In terms of drivetrain, the survey recommended starting with a direct-drive generator.

1.3 Design Process and Report Structure

The result of the design process is a turbine with a nameplate power rating of 22 MW, a rotor diameter of 284 m, and a hub height of 170 m. The turbine was developed cooperatively between teams at DTU and NREL with valuable input and feedback from industry and research collaborators. The main components of the turbine were designed sequentially with multidisciplinary design tools. The rotor was designed using DTU's in-house Aero-Structural Optimization Framework for Wind Turbines (AESOpt) [10] and aeroelastic code HAWC2. NREL's Wind-Plant Integrated System Design and Engineering Model (WISDEM) and Wind Energy with Integrated Servo-control (WEIS) toolchains were used to design the drivetrain, tower, monopile, and semisubmersible floater. The turbine was designed primarily with medium-fidelity aeroelastic modeling in mind and is therefore in this report described to a level appropriate for such modeling approaches.

This report provides an overview of the turbine and documents the design basis and characteristics of each subcomponent in the turbine. Section 2 describes the rotor design and the tools used in the design process. Section 3 describes the design process and properties of the hub, drivetrain, and nacelle. Section 4 describes the tower and monopile designs, and Section 5 describes the semisubmersible floater. Section 6 presents modal analysis and design load evaluations of the two turbine configurations in offshore conditions based on the DTU aeroelastic tools HAWCStab2 and HAWC2.

1.4 Overall Turbine Characteristics

Table 1 summarizes the main properties of the turbine.

Table 1: Overview of the main properties of the IEA 22 MW reference wind turbine

Quantity	Value
Rated elec. power [MW]	22.0
Specific power [$\mathrm{W\,m^{-2}}$]	351.410
Wind class	1B
Rotor orientation	Upwind
Number of blades	3
Control	Variable speed, collective pitch
Cut-in wind speed [$\mathrm{m\,s^{-1}}$]	3.0
Rated wind speed [$\mathrm{m\,s^{-1}}$]	11.0
Cut-out wind speed [$\mathrm{m\,s^{-1}}$]	25.0
Design tip-speed ratio	9.153
Min. rotor speed [rpm]	1.807
Max. rotor speed [rpm]	7.061
Max. blade tip speed [$\mathrm{m\,s^{-1}}$]	105.0
Rotor diameter [m]	284.0
Hub diameter [m]	8.4
Blade length [m]	137.8
Blade prebend [m]	7.0
Blade mass [t]	82.301
Airfoil series	FFA-W3
Blade root diameter [m]	5.8
Rotor precone angle [deg.]	4.0
Shaft tilt angle [deg.]	6.0
Hub height [m]	170.0
Drivetrain	Direct drive
Generator efficiency at rated load [%]	95.4
Hub system mass [t]	120.0
Nacelle assembly mass (excludes hub system) [t]	821.2
Tower mass [t]	1,574
Monopile mass [t]	2,097

1.5 Model Availability

The IEA 22 MW RWT is fully open source, licensed with an Apache 2.0 license, and made available via GitHub at the following address:

- `https://github.com/IEAWindTask37/IEA-22-280-RWT`

The primary file format used to define dimensions and properties of the turbine is the WindIO format [7]. Aero-servo-hydro-elastic input files to model the turbine in HAWC2, HAWCStab2, and OpenFAST are also available in the repository.

1.5.1 Versioning and Issues

The version of the turbine documented in this report is tagged as version 1.0.1. No major changes to the design will be made following its release, but should the authors or the broader community identify inconsistencies or errors in the definition of the turbine, these errors will be fixed and tagged appropriately. When referring to the turbine, it is therefore advised to also cite the specific version used. Users of the turbine are encouraged to use the issue tracking system in the repository to raise issues or questions regarding the turbine.

2 Rotor

This section provides an overview of the design characteristics of the IEA 22 MW RWT rotor design. A preliminary load level investigation is presented, followed by a brief overview of the methodology used in the rotor design process and descriptions of the blade geometry and steady-state rotor performance.

2.1 Preliminary Load-Level Investigations

As an initial step before the detailed rotor design, a study to set the level for the steady-state thrust was carried out. A semi-analytical optimization method is used to establish the optimal relationship between the power coefficient (C_P) and the thrust coefficient (C_T). Using this result for each wind speed independently, the optimal power curve for a given thrust constraint can be found [11]. The approach is used to investigate the impact of a global thrust limit (often referred to as peak shaving) on the annual energy production (AEP). The methodology does not include any information about the blade planform, such as chord and twist, but only information about the loading of the rotor. The model does include operational information such as tip-speed ratio and glide ratio along the span ($C_l/C_d(r)$). It also includes a tip-loss correction in the same way it is included in common blade-element momentum implementations.

The result of the study is shown in Figure 1, where the relative AEP change compared to the design with unconstrained thrust is plotted for a changing level of the relative thrust. The reduction in AEP is relatively small in the beginning and progressively increases with decreasing relative thrust. A good compromise between the loss in AEP and the gain from a lower thrust was found with a decrease in thrust of $\Delta T = -15\%$ (nominal value $T_{ss,\max} = 2.84$ MN) leading to a decrease in AEP of $\Delta AEP = -0.25\%$.
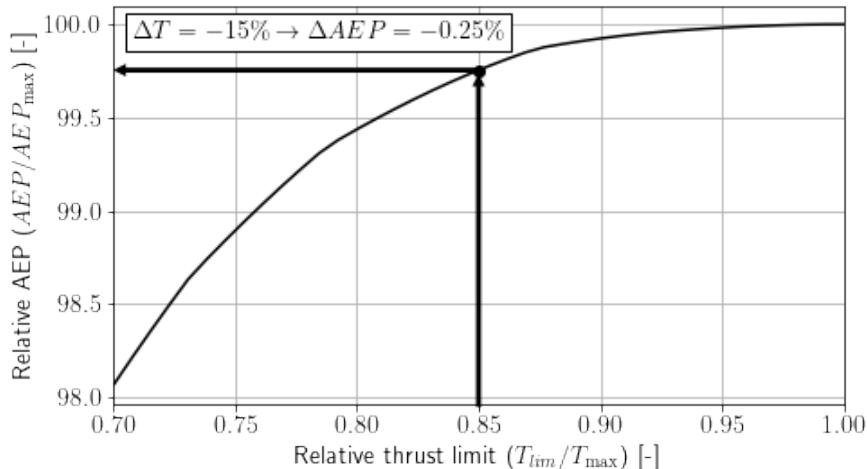
Figure 1: Relative AEP change for varying levels of maximum relative steady-state thrust.

2.2 Aerostructural Rotor Design

2.2.1 Design Method

The rotor was optimized to maximize AEP considering design variables related to aerodynamic blade planform, composite structure, and steady-state operating schedule (tip-speed ratio and blade pitch angle), subject to constraints on blade deflection, blade structural frequencies, blade mass, blade mass moment, blade material strain limits, and loads (rotor thrust and blade root flapwise moment). The mass constraints were determined a priori, based on manual upscaling from various other designs, and suitable constraints of the steady-state thrust and flapwise moment limits were determined as described in Section 2.1. It should be

noted that the design process did not involve higher-fidelity structural modeling of the blade to evaluate failure modes due to events such as buckling. The rudimentary sizing of the root transition piece was based on simple scaling relative to previously published RWTs, and details regarding the bolted interface to the hub were not considered. Note also that the blade structural design does not include added mass from adhesives and other non-load carrying parasitic masses, which could add in the order of 5% extra mass. The authors acknowledge that this should be included in a future update of the design performed at higher fidelity.

The IEA 22 MW rotor was designed using DTU's in-house aerostructural design framework AESOpt [10]. To compute structural properties, the cross-sectional finite element tool BECAS (v4.0) [12, 13] was used. To compute the rotor aeroelastic response, AESOpt solves a nonlinear static aeroelastic problem using the aerodynamic code BEVC (blade-element vortex cylinder) [14–16] and a static multibody solver available in HAWC2 [17] using an anisotropic fully populated matrix beam-element model. Design loads were computed using an empirical model based on the static aeroelastic loads, which is based on the work by Fuglsang and Thomsen [18].

AESOpt uses OpenMDAO v3.x [19] to handle the definition of the optimization problem, workflow, dataflow, and parallelization of simulation cases. This enables efficient use of high-performance computing clusters, with MPI parallelization of both cases within the objective function and the evaluation of finite difference gradients. In this work, the open-source gradient-based interior point optimizer IPOPT [20] is used through the PyOptSparse [21] OpenMDAO driver. AESOpt supports the computation of analytical gradients across all models in the toolchain, but at the time of developing the rotor, this function in AESOpt was not fully validated; instead, central finite differencing was used to compute gradients.

2.2.2   Overall Rotor Characteristics

Table 2 provides an overview of the rotor design characteristics and key rated steady-state loads.

Table 2: Overall characteristics of the rotor. [*] Evaluated using HAWCStab2.

Quantity	Value
Blade mass [t]	82.3
Blade length [m]	137.8
Blade prebend [m]	7.0
Blade precone [deg]	4.0
Blade root diameter [m]	5.8
Blade max. chord [m]	7.2
Max. tip speed [$m\,s^{-1}$]	105.0
Tip-speed ratio [-]	9.15
Rated rotor speed [rpm]	7.06
Rated torque [kN m]	31,465.0
Rated thrust [kN]	2,793.0
Rated blade root flapwise moment [kN m]	79,528.0
Airfoil family	FFA-W3
Minimum airfoil relative thickness	21%
Blade 1st moment mass[*] [$Kg\,m$]	3.033E+06
Blade 2nd moment mass[*] [$Kg\,m^2$]	2.052E+08
Blade 1st flapwise mode[*] [Hz]	0.384
Blade 1st edgewise mode[*] [Hz]	0.520
Blade 1st torsional mode[*] [Hz]	3.961

2.2.3 Material Characteristics

The materials used in the present project are adapted from NREL's Big Adaptive Rotor project and described in detail in E. Camarena et al [22]. In Tables 3 and 4, the stiffness properties and strength capacity are listed. Note that the strength properties reported here do not include the partial safety factor (PSF) of 1.74 used in [22].

Table 3: Material stiffness properties used in the design process. Legend: E Young's modulus, ν Poisson's ratio, G shear stiffness, ρ density. For further details on the materials see Camarena et al. [22].

Quantity	gelcoat	glass_uniax	carbon_uniax	glass_biax	glass_triax	medium_density_foam
E_1 [Pa]	3.440E+09	4.370E+10	1.400E+11	1.102E+10	2.821E+10	1.425E+08
E_2 [Pa]	-	1.650E+10	9.100E+09	1.102E+10	1.624E+10	-
E_3 [Pa]	-	1.545E+10	9.100E+09	1.605E+10	1.584E+10	-
ν_{12} [-]	3.000E−01	2.620E−01	3.133E−01	6.881E−01	4.975E−01	3.194E−01
ν_{13} [-]	-	2.640E−01	3.133E−01	1.172E−01	1.809E−01	-
ν_{23} [-]	-	3.500E−01	4.707E−01	1.172E−01	2.748E−01	-
G_{12} [Pa]	1.323E+09	3.265E+09	4.131E+09	1.323E+10	8.248E+09	5.400E+07
G_{13} [Pa]	-	3.495E+09	4.131E+09	3.487E+09	3.491E+09	-
G_{23} [Pa]	-	3.480E+09	2.689E+09	3.487E+09	3.491E+09	-
ρ (kg m^{-3})	1.235E+03	1.940E+03	1.600E+03	1.940E+03	1.940E+03	1.300E+02

Table 4: Material ultimate tensile strength (Xt) and ultimate compressive strength (Xc) properties. In the design process, only the $_{11}$ direction was considered. The strength properties do not include partial safety factors.

Quantity	gelcoat	glass_uniax	carbon_uniax	glass_biax	glass_triax	medium_density_foam
Xt_{11} [Pa]	1.288E+08	1.114E+09	2.236E+09	1.206E+08	7.580E+08	3.624E+06
Xt_{22} [Pa]	-	6.629E+07	6.629E+07	1.206E+08	1.330E+08	-
Xt_{33} [Pa]	-	0.000E+00	0.000E+00	1.206E+08	0.000E+00	-
Xc_{11} [Pa]	1.514E+08	6.450E+08	1.528E+09	1.230E+08	5.970E+08	2.720E+06
Xc_{22} [Pa]	-	1.430E+08	1.430E+08	1.230E+08	3.040E+08	-
Xc_{33} [Pa]	-	0.000E+00	0.000E+00	1.230E+08	0.000E+00	-

Partial safefy factors (PSFs) used in the strength analysis of the blade are based on Germanischer Lloyd "Guideline for the certification of wind turbines" (section 5.5.2.1 page 5-20). PSFs are computed as the product of a partial safety factor and reduction elements as listed in Table 5 according to Equation 1.

Constant	Value	Description
$\gamma M0$	1.35	Partial safety factor
C1a	1.35	Influence of ageing
C2a	1.1	Temperature effect
C3a	1.1	Laminate produced by prepregs, winding techniques, pultrusion or resin infusion method
C4a	1.0	Post-cured laminate

Table 5: Material partial safety factors used in the design process.

$$\gamma Ma = \gamma M0 \prod_i C_{ia} \tag{1}$$

This results in a total PSF of 2.205 applied to evaluate the maximum strain failure criterium of the blade, presented in Section 2.3. Note that the chosen PSFs are conservative compared to those used by Camerena et al [22], and likely also conservative compared to common practice in industrial designs.

2.2.4 Airfoil Data

For this rotor design, the FFA-W3 airfoil family was used (Figure 2). Airfoil data used for the aeroelastic simulations were based on 2D computational fluid dynamics (CFD) simulations using the incompressible 2D CFD code EllipSys2D [23–25] computed at Reynolds numbers representative of normal operating conditions for the spanwise locations of each airfoil in the range of Re = 8E+6 to Re = 18E+6. Airfoil data based on wind tunnel measurements at these Reynolds number ranges are not available for the FFA-W3 airfoil family, and therefore the 2D CFD results were used without consideration of possible discrepancies between numerical and wind tunnel measured performance of the airfoils, for example related to the maximum lift coefficient, and resulting stall margins in operation. Polars used in the aeroelastic simulations presented in Section 6 are a mix of fully turbulent simulations and simulations taking into account laminar-to-turbulent transition, mixed with a ratio of 30% and 70%. The spanwise locations of each airfoil are shown in the center-left plot of Figure 12 and are listed in the WindIO yaml on GitHub. The WindIO file also lists the computed turbulent and transitional polars. Figures 3 to 10 show the individual polars with lift coefficient vs. angle of attack and lift-to-drag ratio vs. lift coefficient. Figure 11 shows the full 360° polars, which were extrapolated using the tool AirfoilPreppy [26]. For airfoil relative thicknesses greater than 48%, linear interpolation was used between the 48% airfoil and the cylinder at blade root. The cylinder adopted a lift coefficient of 0.0 and a drag coefficient of 0.35. Finally, note that the airfoil data in WindIO and in this report do not include application of an engineering 3D flow correction model. A 3D correction based on the Snel model is activated by default in HAWC2 [17]. The airfoil input files to OpenFAST include a 3D correction based on the Du-Selig model [27].
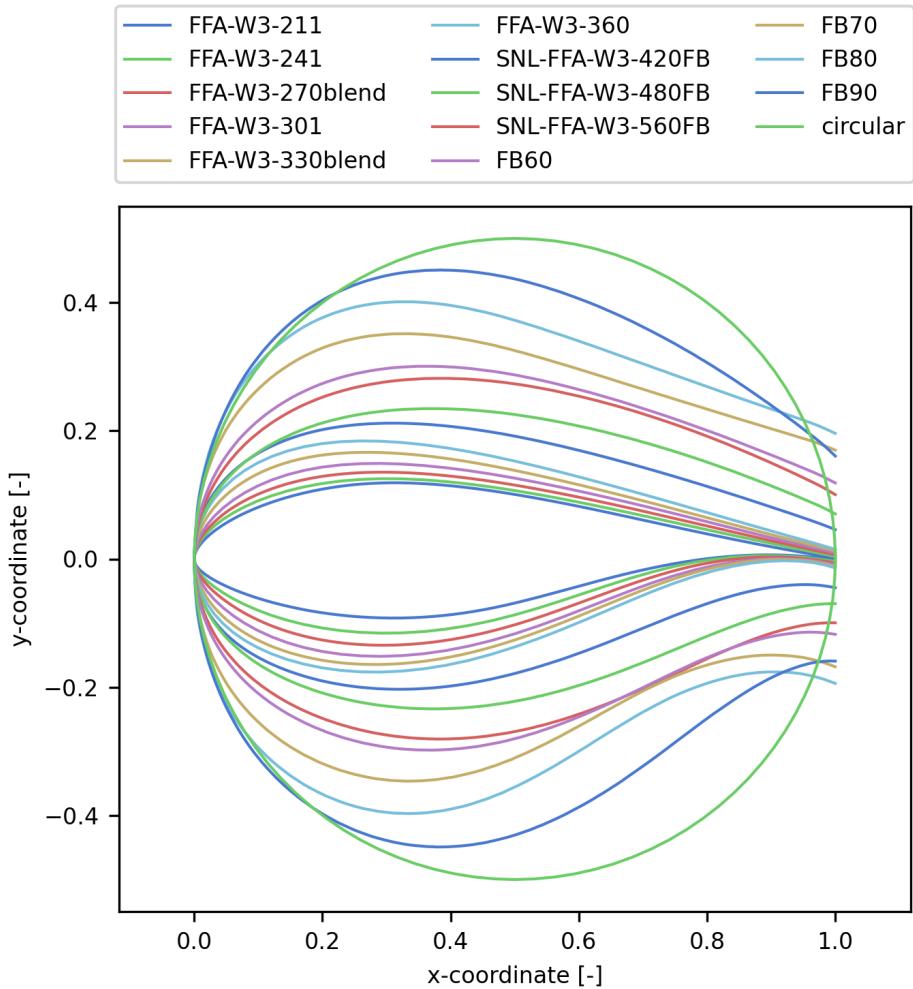
Figure 2: Contours of the FFA-W3 airfoil family, including two intermediate thicknesses (FFA-W3-xxxblend), generated for compatibility. Thick flatback airfoils were generated using interpolation and adjusted manually. The naming of the airfoils points to the relative thickness (211 - 21.1%, 241 - 24.1%, and so on).
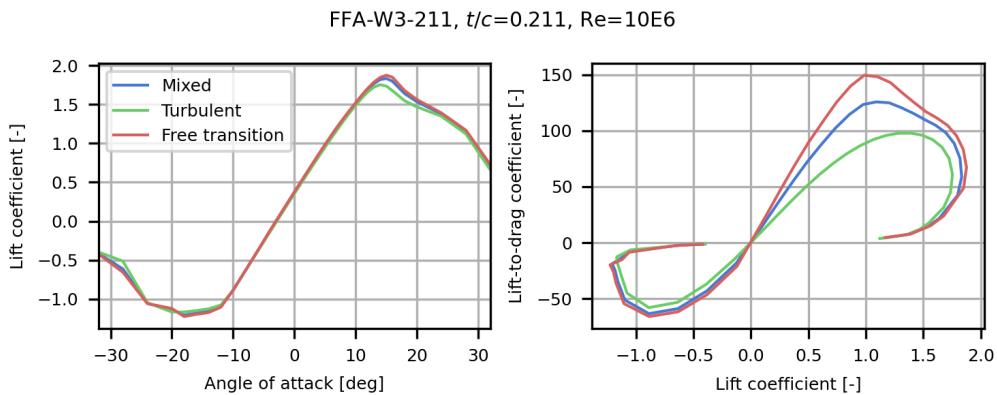
Figure 3: Airfoil data for the 21.1% relative thickness (t/c) FFA-W3-211 airfoil computed at a Reynolds number of 10E+6.
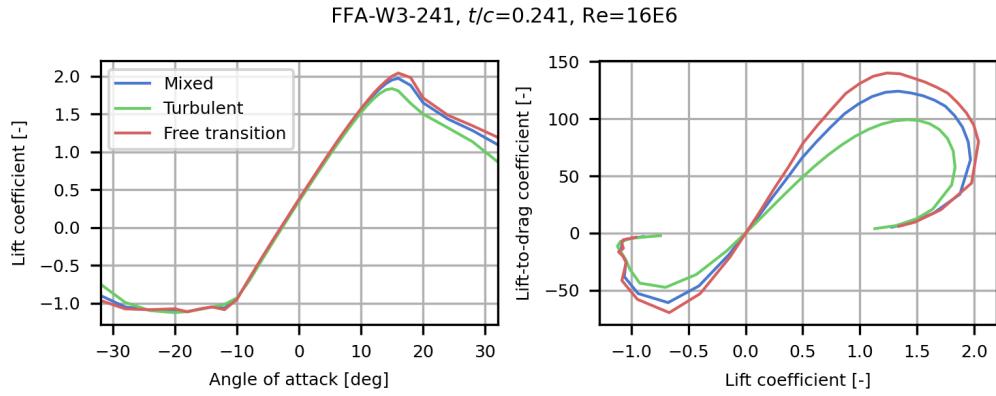
Figure 4: Airfoil data for the 24.1% relative thickness (t/c) FFA-W3-241 airfoil computed at a Reynolds number of 16E+6.
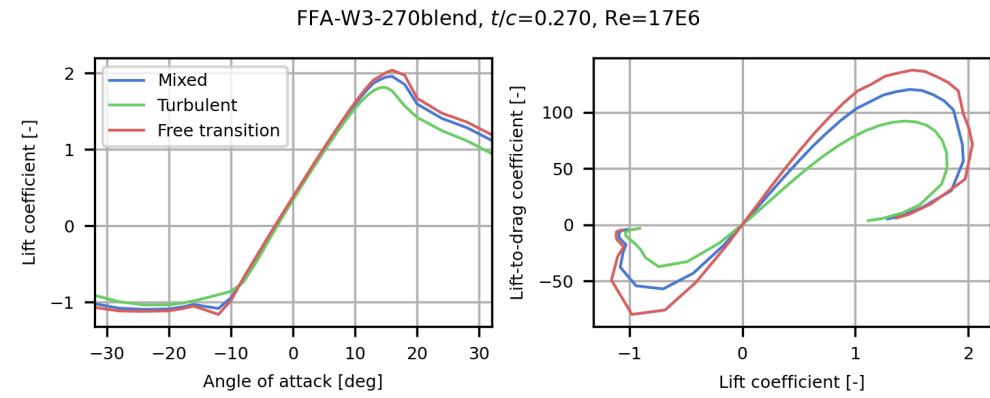
Figure 5: Airfoil data for the 27.0% relative thickness (t/c) FFA-W3-270blend airfoil computed at a Reynolds number of 17E+6.
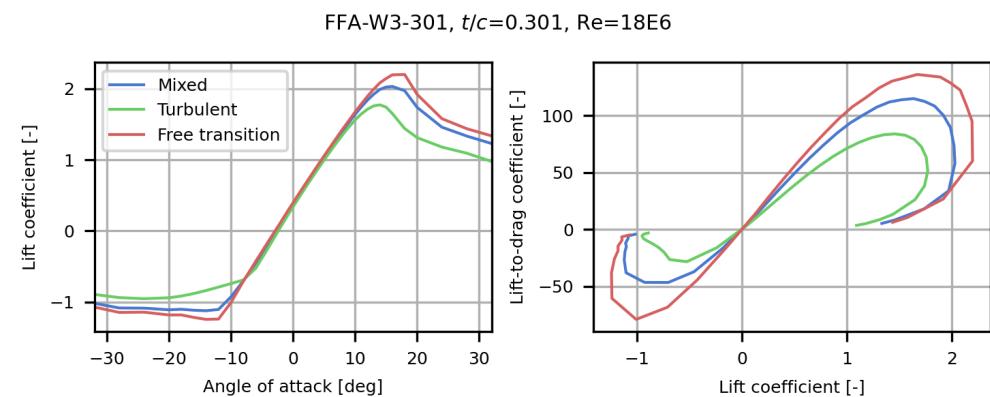
Figure 6: Airfoil data for the 30.1% relative thickness (t/c) FFA-W3-301 airfoil computed at a Reynolds number of 18E+6.
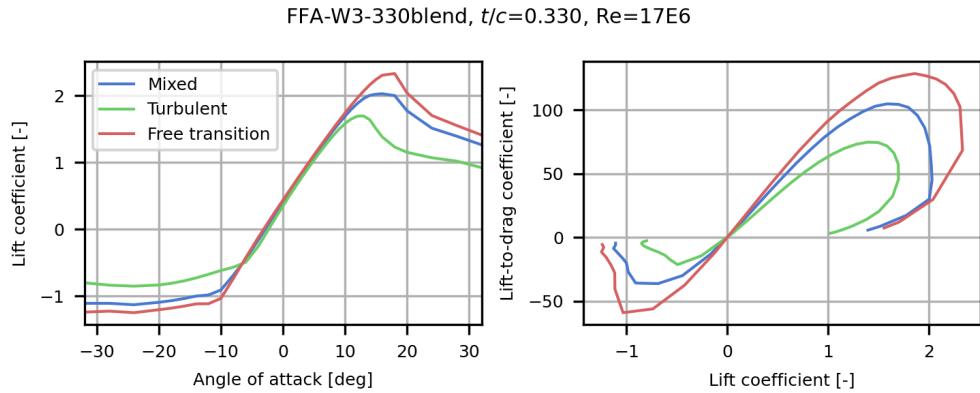
Figure 7: Airfoil data for the 33.0% relative thickness (t/c) FFA-W3-330blend airfoil computed at a Reynolds number of 17E+6.
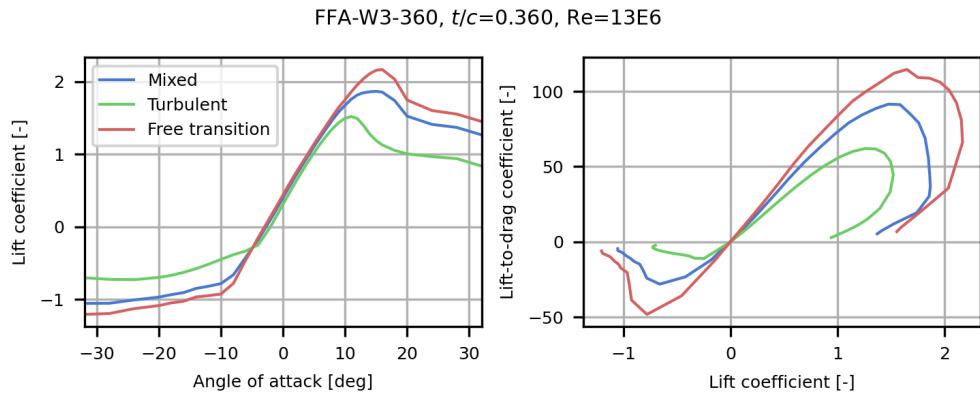
Figure 8: Airfoil data for the 36.0% relative thickness (t/c) FFA-W3-360 airfoil computed at a Reynolds number of 13E+6.
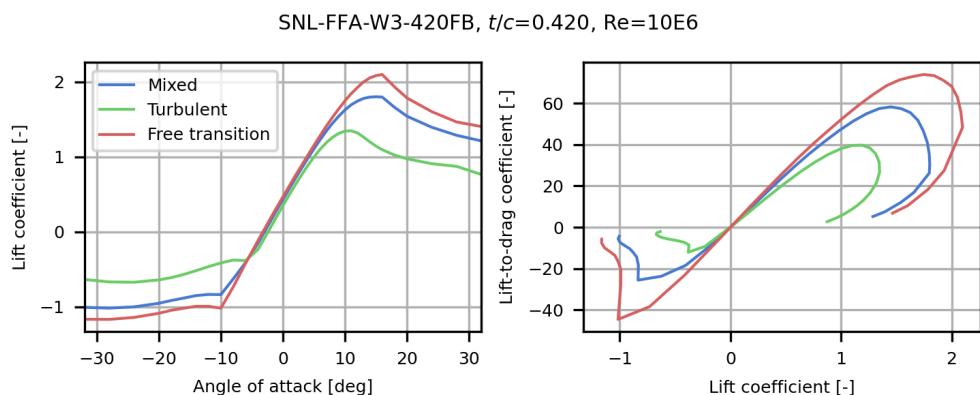
Figure 9: Airfoil data for the 42.0% relative thickness (t/c) SNL-FFA-W3-420FB airfoil computed at a Reynolds number of 10E+6.
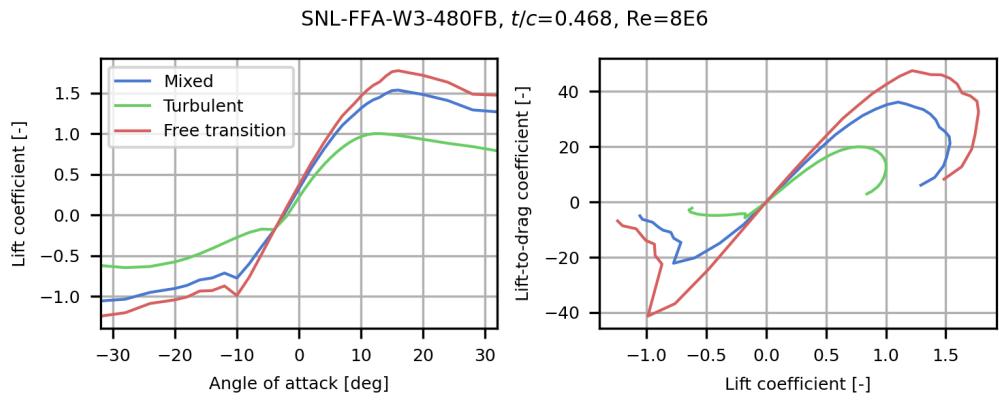
Figure 10: Airfoil data for the 48.0% relative thickness (t/c) SNL-FFA-W3-480FB airfoil computed at a Reynolds number of 8E+6.
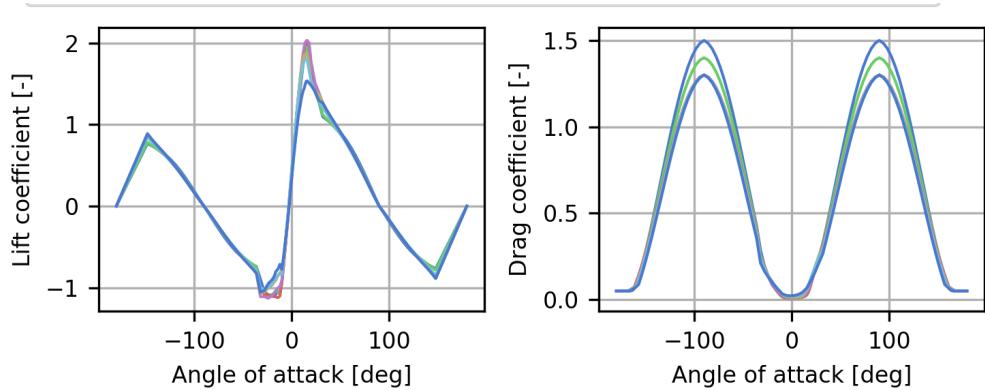
Figure 11: Airfoil lift and drag coefficients for the full set of polars used in the aeroelastic simulations.

2.2.5 Geometric Definition of the Blade

Figure 12 shows some of the main geometrical quantities as function of dimensionless spanwise variable (referred to as "spanwise grid"). The chord was limited to a maximum of 7.2 m in the design process, and a root diameter of 5.8 m was chosen. Blade prebend was constrained to not exceed 7 m at the tip. The twist was defined as positive for a nose-down rotation of the local cross section. The relative thickness distribution was constrained in the design process to ensure that the relative thickness did not become too high, which could negatively influence the blade performance, especially under soiled or worn surface conditions. The normalized chordwise offset was used as part of the lofting process and is defined as the distance from the leading edge to the blade twist axis, normalized with local chord, and named "pitch axis" in the WindIO ontology. More details are available in the online documentation of WindIO. Figure 13 shows two plots of the resulting lofted blade.
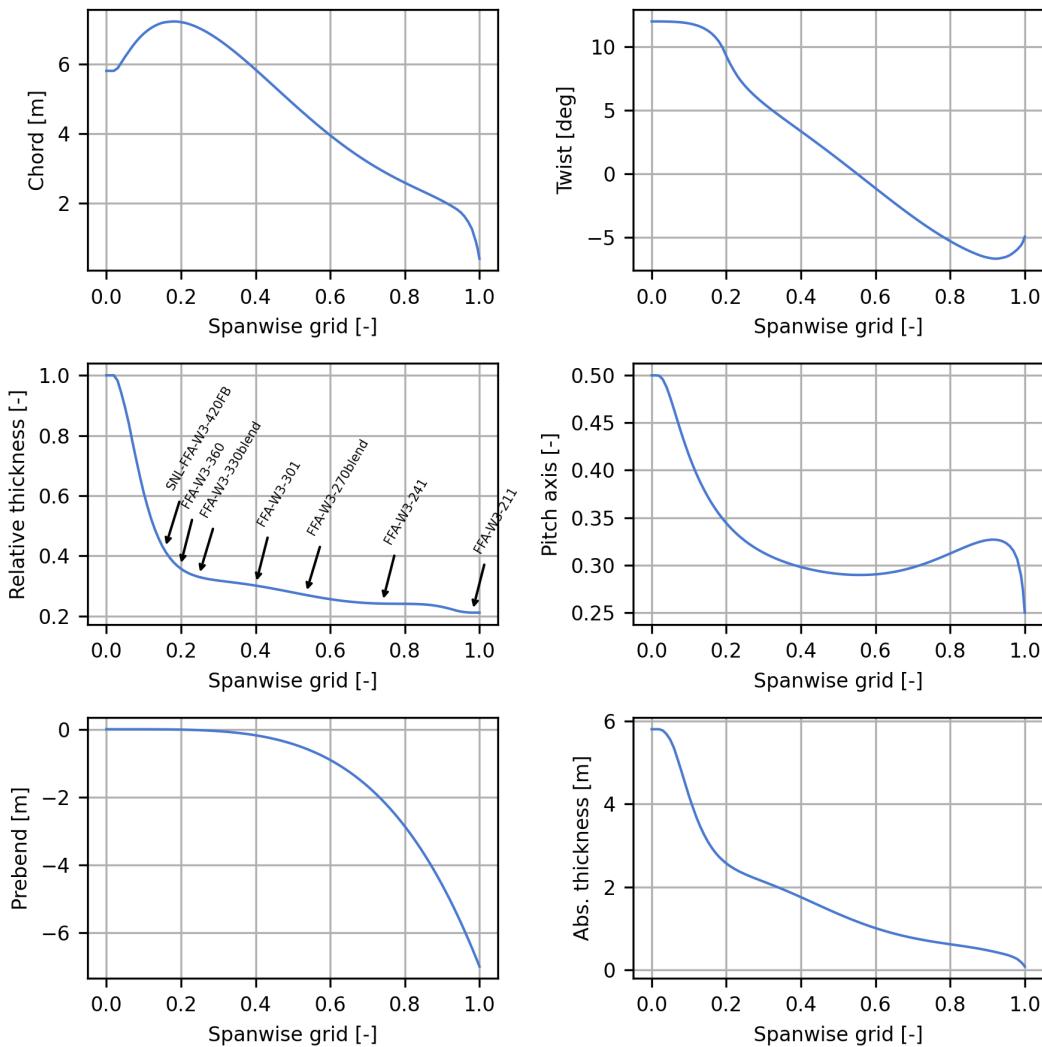
Figure 12: Blade planform of the IEA 22 MW RWT blade. A blade geometric twist of 0 degrees corresponds to a pitch angle of 0 degrees.

2.2.6 Structural Characteristics of the Blade

The structural layout of the IEA 22 MW RWT blade follows a conventional layout with an inner and outer glass triaxial skin covering the full blade. The load-carrying structure includes two spar caps made of pultruded carbon fiber placed along the suction and pressure sides of the blade connected with two
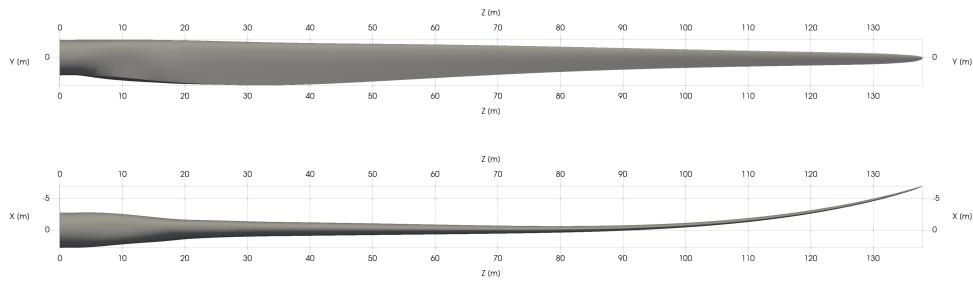
Figure 13: Top and side views of the IEA 22 MW RWT blade.
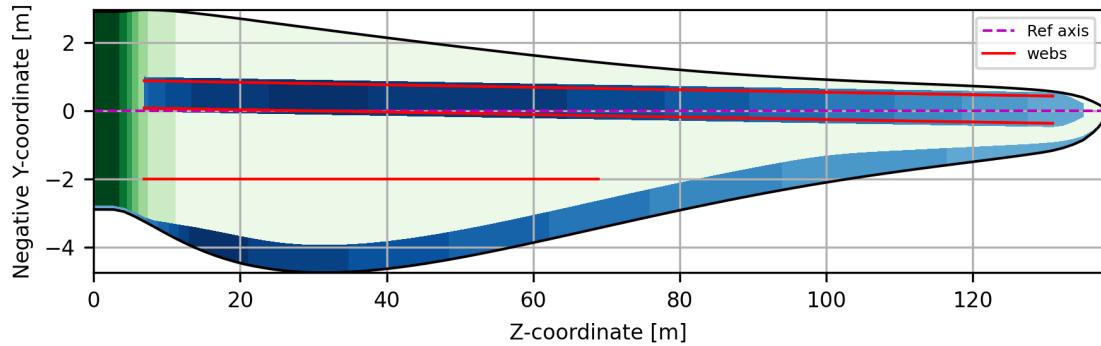
Figure 14: Top-view schematic of the blade showing internal structural layout. The green shading represents the thickness of the outer shell skin. The blue shading represents the thickness of unidirectional spar caps (made of pultruded carbon) and trailing edge reinforcement (made of unidirectional glass).

shear webs made of sandwich structures with biaxial glass fiber and foam. A third aft shear web extends approximately 50% of the span from the root. Uniaxial glass fiber is placed in the leading and trailing edges to carry edgewise loads. Figure 14 shows a top view of the blade and its internal structural layout. The carbon fiber spar cap is shown in blue, and the main and aft shear webs are shown in red. The glass uniaxial trailing edge reinforcement region is also shown in blue. Figure 15 shows cross-sectional meshes at a range of spanwise positions used for computing stiffness properties with the cross-sectional finite element tool BECAS. Figure 16 shows the thicknesses and widths of the main laminate regions in the blade: skin (triaxial), trailing edge and leading edge reinforcements (glass uniaxial), and the spar cap (carbon uniaxial).

Table 6 lists the first 10 modal structural frequencies of the blade at standstill (excluding aerodynamics and gravity) computed using HAWCStab2 [28]. For full turbine aeroelastic modal analysis, see Section 6. Figures 17, 18, and 19 show the blade beam properties defined in the WindIO reference system. The stiffness and inertia properties are computed using BECAS. The full 6×6 stiffness and inertia matrices, appropriately transformed into code-specific reference frames, are used in both HAWC2 computations (full populated matrix = 1) and in OpenFAST using BeamDyn.
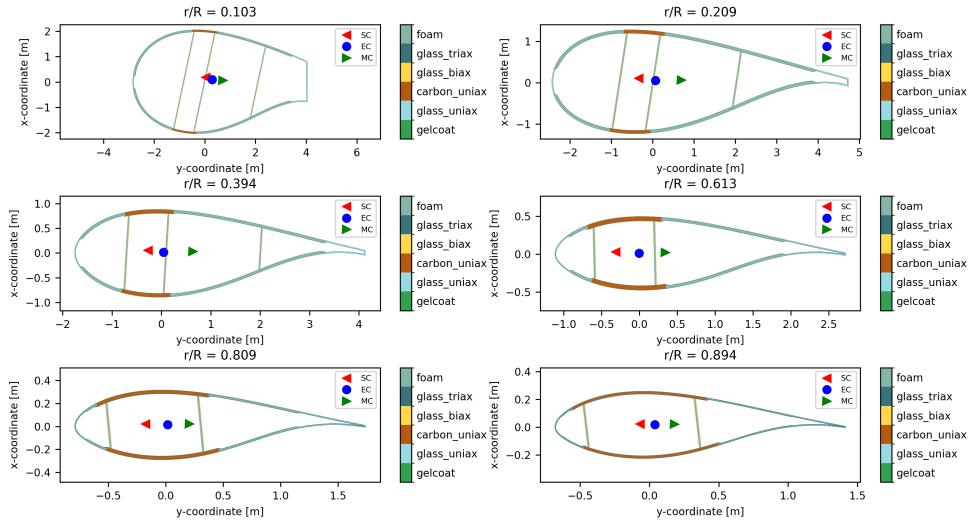
Figure 15: Cross-sectional views of a mesh for the sections at r/R = [0.1, 0.3, 0.6, 0.9] used to compute stiffness properties of the blade. The origin of the coordinate system of the cross-sections corresponds to the blade reference axis, as defined in the WindIO definition of the blade.

Table 6: Structural frequencies of the blade clamped at its root

Mode Name	Frequency [Hz]
First flapwise mode	0.384
First edgewise mode	0.520
Second flapwise mode	1.059
Second edgewise mode	1.445
Third flapwise mode	2.218
Third edgewise mode	3.118
Fourth flapwise mode	3.739
First torsional mode	3.957
Fourth edgewise mode	5.274
Fifth flapwise mode	5.681
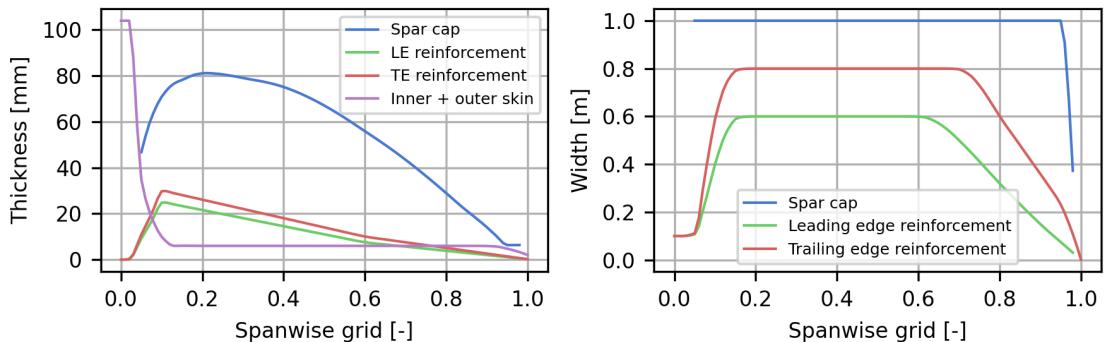
Figure 16: Material thicknesses and widths of primary composite layers in the blade.
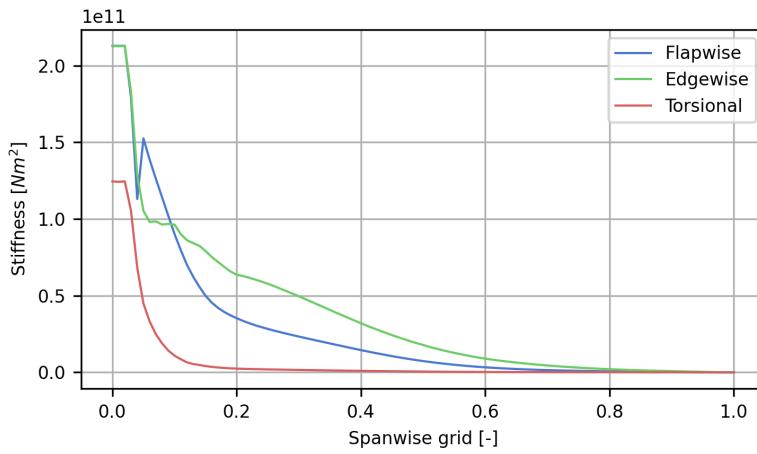
Figure 17: Blade flapwise, edgewise, and torsional stiffnesses as a function of blade span defined in the WindIO reference frame.
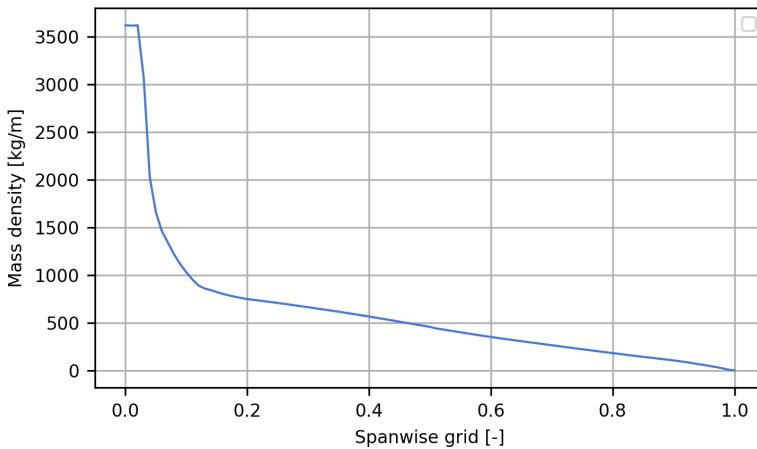
Figure 18: Mass density along the blade.
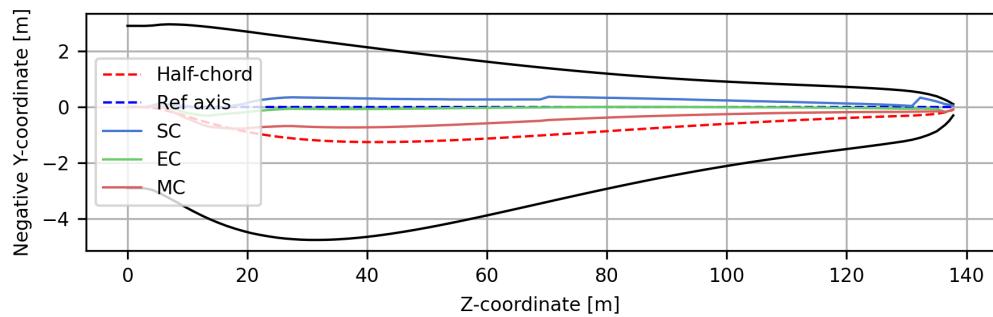
Figure 19: Shear, elastic, and mass centers as a function of blade span.

2.2.7 Rotor Performance

The steady-state operating schedule of the rotor is defined in Table 7 optimized for the turbine without tower top tilt, and for uniform inflow conditions neglecting the effects of gravity. These values were optimized based on the solver HAWC2 and are listed in the GitHub repositories, together with datasets corresponding to other aeroelastic solvers such as OpenFAST.

Table 7: Steady-state operating schedule for the rotor

Wind Speed [$\mathrm{m\,s^{-1}}$]	Pitch [deg]	Rotor Speed [rpm]
3.0	0.58064	1.84662
4.0	0.33798	2.46216
5.0	0.00915	3.07770
6.0	−0.33797	3.69324
7.0	−0.63879	4.30878
8.0	−0.97996	4.92432
9.0	−1.32680	5.53986
10.0	0.73192	6.15540
11.0	2.42859	6.77094
12.0	5.09471	7.06110
13.0	7.26585	7.06110
14.0	9.01413	7.06110
15.0	10.53731	7.06110
16.0	11.91818	7.06110
17.0	13.20451	7.06110
18.0	14.42148	7.06110
19.0	15.58471	7.06110
20.0	16.70423	7.06110
21.0	17.78860	7.06110
22.0	18.84311	7.06110
23.0	19.87209	7.06110
24.0	20.87848	7.06110
25.0	21.86473	7.06110

Figure 20 shows the steady-state rotor performance computed with AESOpt. At low wind speeds, the rotor operates at an almost constant power coefficient close to 0.5 and a thrust coefficient of 0.8. The rotor thrust and flapwise moment are reduced near the rated wind speed due to the introduction of peak shaving by pitching the blades towards feather in this region. The flapwise moment coefficient, C_{M-x}, defined as $C_{M-x} = \frac{M_x}{0.5\rho U_{inf}**2\pi R^3}$, is constant between the cut-in wind speed and 9 m/s at approximately C_{M-x}=0.18, and reducing linearly in the peak shaving region until 11.5 m/s, This is combined with an increasing torsional response towards feather as a function of wind speed, with a maximum torsion of approximately 5.5° at $11\,\mathrm{m\,s^{-1}}$. Figure 21 shows the blade tip deflection and torsion against wind speed. From Figures 20 and 21 it can be observed that the tip deflection constraint with an upper limit of 20 m was in fact an active constraint along with the flapwise moment that was constrained to -80E3 $kN\,m$, whereas the rotor thrust constraint was not active. Using a combination of peak shaving and bend-twist coupling as part of the design process allows for an aerodynamically more efficient and lighter blade because of the lower loads and deflections resulting from this control strategy. Compared to an operational control strategy with no peak shaving, the thrust and flapwise moment are reduced by approximately 12%, resulting in a 0.5% loss of AEP.

Figure 22 shows a series of plots of the distributed loads along the blade. At maximum chord, the blade operates at high lift coefficients at $C_l > 1.7$, which considering 3D effects is achievable, but could for robustness require vortex generators, which however, is not considered in the present design. Mid-span C_l reduces to between 1.2 and 1.3, which results in a quite large margin to C_{l-max}. Particularly at low wind speeds, the outer part of the blade at r/R=0.9 operates at quite high lift coefficients of C_l=1.55, which leaves a stall margin of $\Delta C_l = 0.285$ relative to the turbulent polar (see Figure 4). In the plots of axial induction and local thrust coefficient, it is evident that the spanwise distribution of loading is high at lower wind speeds;

at wind speeds up to 9 m s^{-1}, the tip is unloaded purely due to the torsional deformation while the inboard part of the blade remains highly loaded. Above 9 m s^{-1}, the overall loading of the blade is reduced through pitching towards feather with a thrust coefficient of 0.7 at 10 m s^{-1} and 0.6 at 11 m s^{-1}.
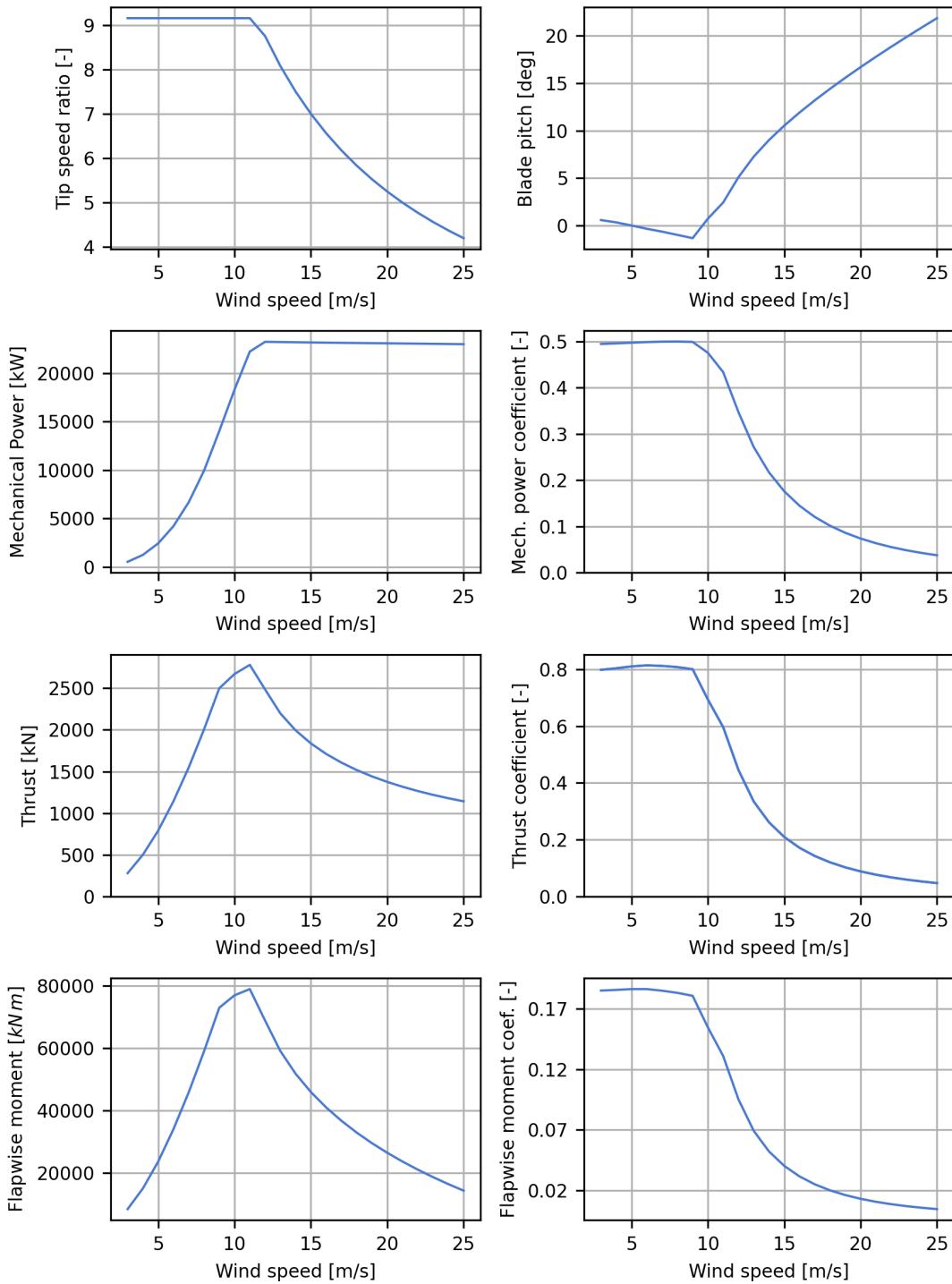
Figure 20: Steady-state rotor performance metrics for the IEA 22 MW RWT.
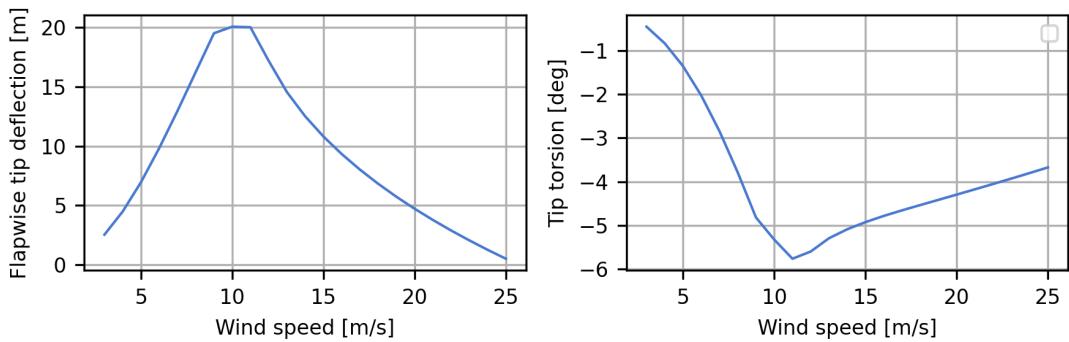
Figure 21: Steady-state tip deflection and torsion relative to the unloaded geometry for the IEA 22 MW RWT.
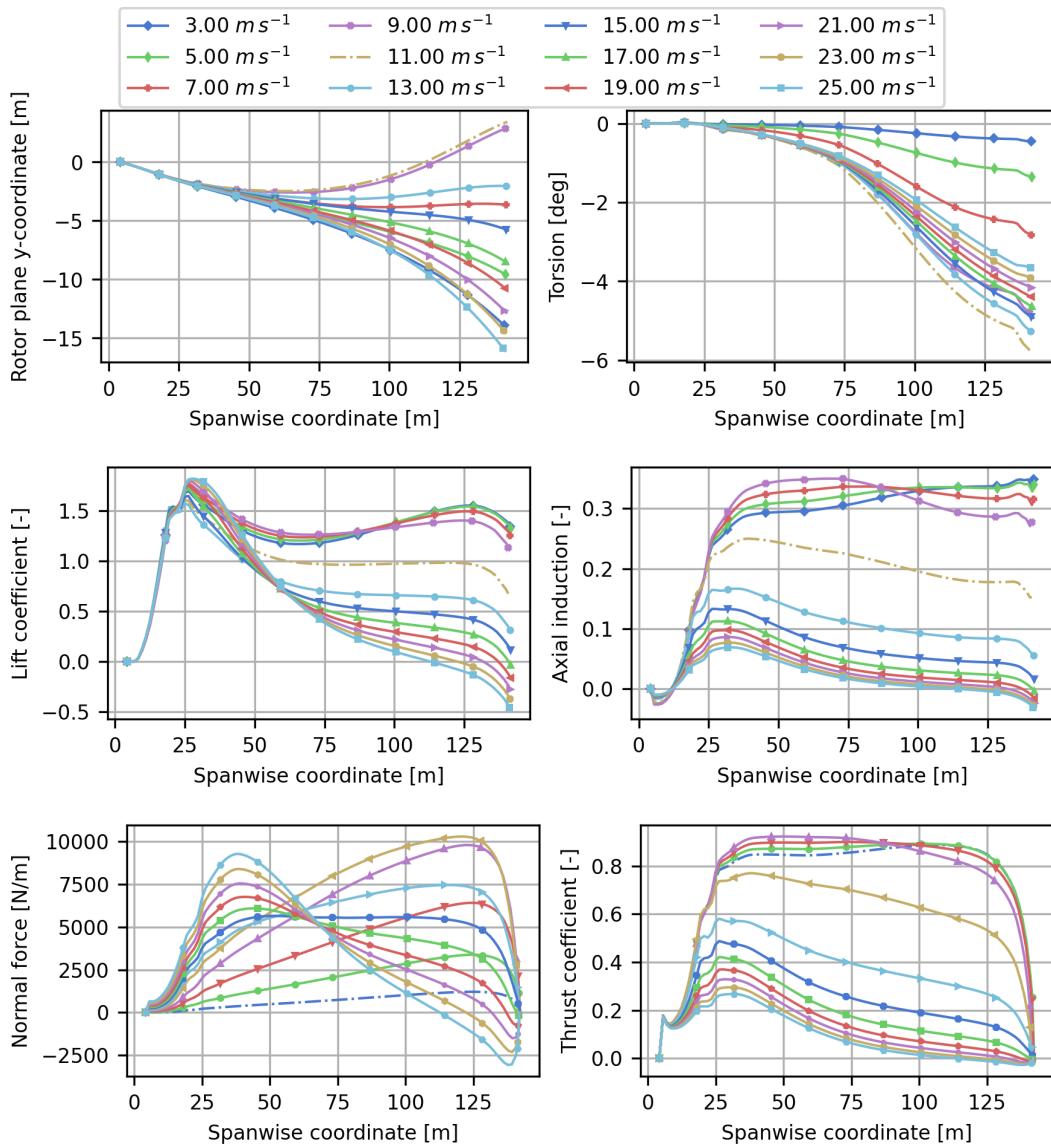
Figure 22: Quasi-steady blade distributed loading for a range of wind speeds.

2.3 Strain Analysis

Figure 23 shows the minumum and maximum values of the blade design loads used to evaluate strain, which are based on the HAWC2 design loads evaluation described in Section 6, and documented further in Appendix A. A total of 12 load cases were evaluated for each cross-section corresponding to the minimum and maximum values of each load component (3 forces, 3 moments). The computed peak root flapwise moment was approximately $-175 \, \mathrm{MN \, m}$, and the edgewise moment was $69 \, \mathrm{MN \, m}$. The envelope of maximum and minimum strain and distributions of strain failure indices for the 12 cases are plotted in Figure 24. A maximum strain of $4517 \, \mu \, epsilon$ and a minimum of $4420 \, \mu \, \varepsilon$ is predicted which occurs on the inboard part of the blade, close to the maximum chord location. As can be observed, the strain failure index does not reach 1.0, meaning that strain is not an active constraint in the design. Figures 25 and 26 show contours of strain and strain failure index, respectively, for selected sections along the blade for a load case with peak pressure toward suction side flapwise loading.
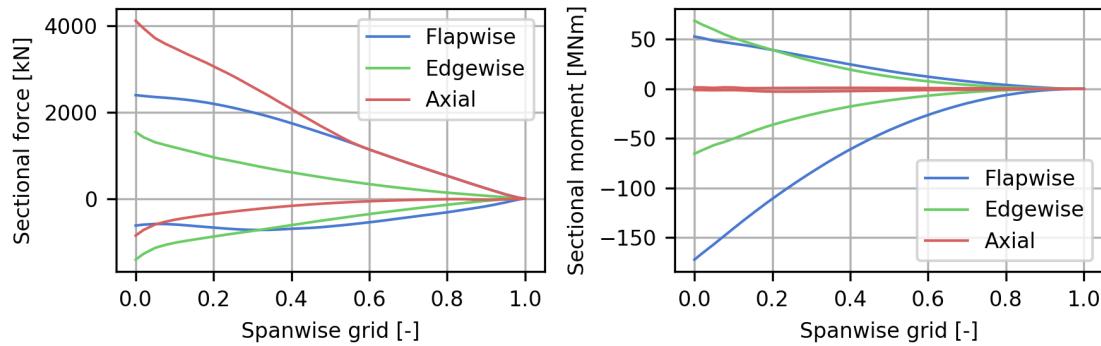
Figure 23: Internal flapwise, edgewise, and axial forces (left) and moments (right) based on HAWC2 design loads analysis (including a PSF of 1.35) as reported in Section 6.
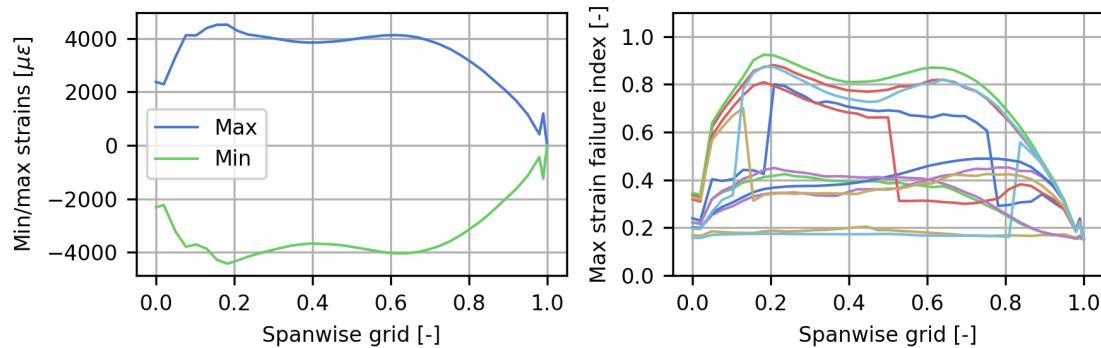
Figure 24: Maximum and minimum strains (left) and strain failure indices for the 12 individual loading directions evaluated (right).
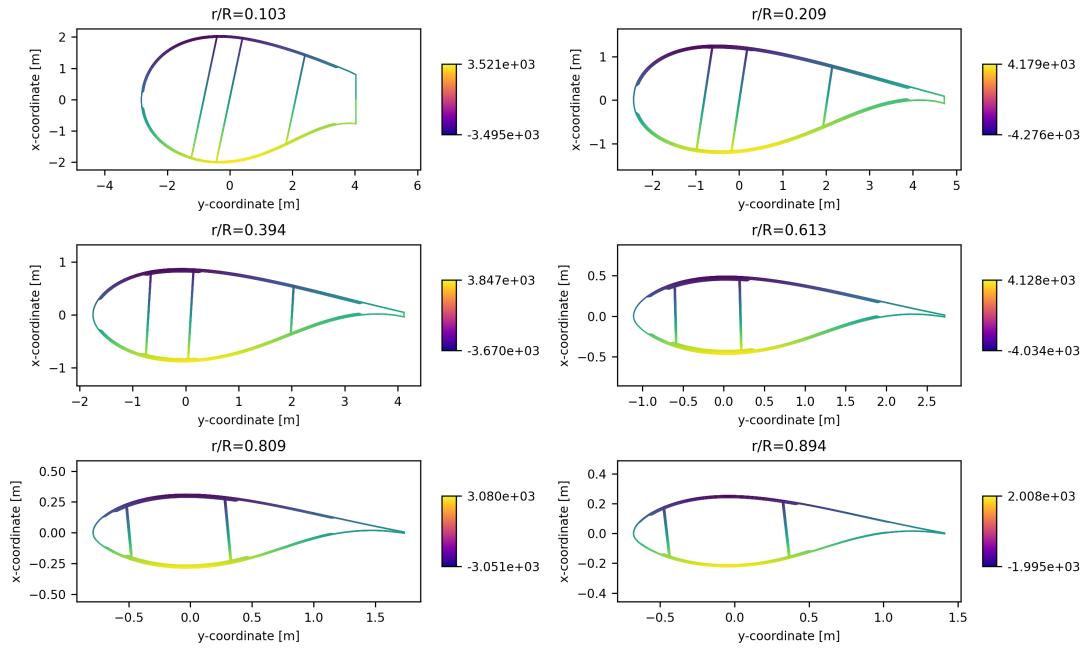
Figure 25: Cross sections with contours of strain for a case with peak pressure toward suction side flapwise loading. The origin of the coordinate system of the cross-sections corresponds to the blade reference axis, as defined in the WindIO definition of the blade.
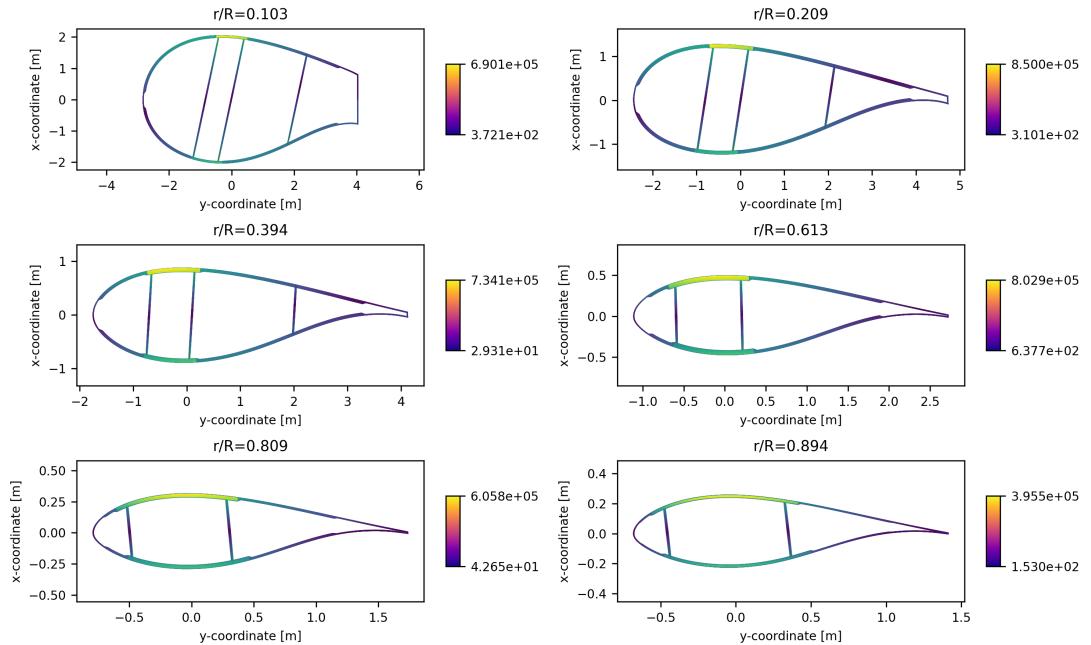
Figure 26: Cross sections with contours of strain failure index for the case with peak pressure toward suction side flapwise loading. The origin of the coordinate system of the cross-sections corresponds to the blade reference axis, as defined in the WindIO definition of the blade.

2.4 Structural Damping

The structural damping of the blade is tuned to achieve a damping ratio, noted ζ, of 0.5% on the first flapwise and first edgewise modes, and a ζ of 2% on the first torsional modes. OpenFAST currently adopts stiffness proportional formulations for structural damping, and so higher-order modes are characterized by higher damping values. The solver HAWC2 has both inertia and stiffness proportional terms for structural damping, but in this model only the latter are currently used. The inputs μ to the stiffness-proportional models of OpenFAST and HAWC2 are listed in Table 8.

Damping	Flap	Edge	Torsion
ζ (%)	0.5	0.5	2.0
δ (%)	3.14	3.14	12.6
f (Hz)	0.39	0.50	4.35
μ OpenFAST (-)	4.05E−3	3.15E−3	0.14E−3
μ HAWC2 (-)	4.25E−3	2.85E−3	1.19E−3

Table 8: Values of target damping ratio ζ, target logarithmic damping δ, blade natural frequencies f in Hz, and inputs to the stiffness-proportional damping formulation μ in the three primary directions.

As a reminder, ζ and the corresponding values of δ are computed as

$$\delta = \frac{2 \cdot \pi}{\sqrt{(\frac{1}{\zeta})^2 - 1}} \tag{2}$$

whereas μ is computed as

$$\mu = 2 \cdot \frac{\zeta}{\omega} \tag{3}$$

where ω is the natural frequency of the blade in rad s^{-1} (f is the natural frequency of the blade in Hz). Note that the μ values of OpenFAST and HAWC2 differ slightly in flapwise and edgewise directions because of differences in the formulation of structural damping. A more marked discrepancy is observed in the torsional μ. The difference is caused by the different impact of coupling terms in the two solvers. The torsional μ in OpenFAST was set manually to achieve a ζ of 2% on the first torsional mode and does not respect Equations 2 and 3.

3   Hub, Drivetrain, and Nacelle

The 22 MW RWT mounts a direct-drive layout with a permanent-magnet, synchronous, radial flux genera-
tor in a simple and compact nacelle layout. The same configuration was adopted in the 15 MW RWT [6],
and again selected for the 22 MW RWT design through a survey of participants in IEA Wind Tasks 37 and
55. Direct-drive wind turbine generators offer a number of advantages over geared drivetrains such as fewer
parts, lower complexity, and higher reliability. On the other hand, the direct coupling of the generator at very
low speeds requires large physical dimensions and higher mass, which can incur transportation, assembly,
and servicing challenges. Countering these challenges involves an optimal balance of generator placement,
main shaft bearing support, rotor-stator support structure and architecture selection, and ancillary compo-
nent interfaces, among other considerations [29, 30]. One notable difference between the 22 MW design
presented here and prior reference turbines is the shift from surface-mounted permanent magnets to interior
permanent magnets, which is discussed in greater detail in Section 3.2.

Figure 27 shows a sketch describing the layout of the drivetrain. The assembly consists of a hub shaft that
supports the three blades and is connected to the generator rotor, which is mounted on two main bearings
housed on a stationary turret. The turret is cantilevered from the bedplate and supports the rotating parts
together with the generator stator. The bedplate transfers the loads to the tower. Not shown is the larger
nacelle housing, which would contain other components such as the power electronics, cooling equipment,
etc.

NREL's systems engineering framework WISDEM was used to design the various components using the
DrivetrainSE module. The generator also went through a higher-fidelity design verification analysis in the
commercial ALTAIR Flux software. The next subsections elaborate on the detailed design of the various
components. The full mass breakdown of the nacelle and its equivalent rigid-body properties are discussed
in Section 3.5.
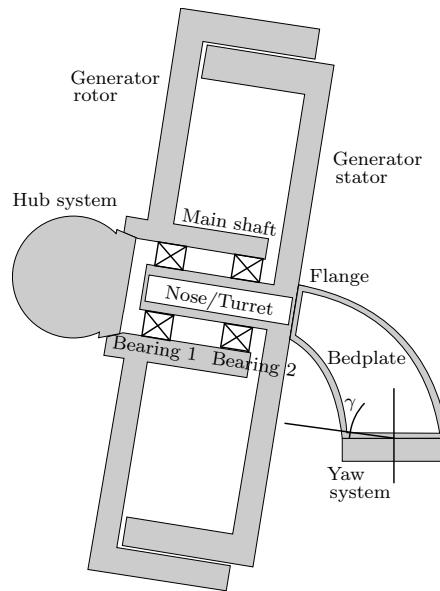
Figure 27: Drivetrain layout of the 22 MW RWT (not to scale).

3.1   Hub System

The hub system consists of the spherical hub connecting the three blades to the main shaft, the spinner,
and the pitch system for each blade. The design of the spherical hub is based on a simple shell model
with cutouts for the blades and the main flange. The hub diameter is set to 8.4 m. The value was set
to accommodate the blade root diameter of 5.8 m. The thickness of the hub shell is sized to withstand
the moment generated in an emergency shutdown event. The simplified model estimates the maximum
moment by assuming that the rotor spinning at rated speed, equal to 7.1 rpm, is brought to a halt in 5 s. No

aerodynamic forcing is included in the calculations. The maximum allowable stress of 44 MPa is obtained by dividing the yield stress of the steel, taken to be 265 MPa, by a stress concentration factor of 3 and a generic safety factor of 2. The resulting thickness of the hub shell is estimated to be 21 mm. The main flange has an outer diameter of 5.04 m (60% of the hub outer diameter), an inner diameter of 4.03 m (80% of the flange outer diameter), and a thickness of 128 mm (6 times the shell thickness). The total mass of the hub shell, excluding spinner and pitch system, is 40 t, and its center of mass is located 3.5 m upwind of the main flange along the shaft axis.

The spinner is assumed to be made of uniaxial glass fiber composite. DrivetrainSE sets the spinner diameter to 1 m greater than the hub, and the wall thickness is set to resist a storm speed of 70 m s^{-1}. The spinner is curved, but for calculation purposes a stress equation valid for a flat plate with simply supported edges is adopted. The load is assumed equal to the extreme gust pressure load,

$$\sigma = \frac{0.75 \cdot P \cdot b^2}{X_t^2 \cdot (1.61 \cdot (b/D_s)^3 + 1)},$$
(4)

where σ is the stress in the spinner, P is the pressure applied to the spinner, b is the width of the equivalent panel forming the spinner, X_t is the maximum allowable tensile strength, and D_s is the diameter of the spinner.

The final mass of the spinner is 3.0 t. This value includes the support metal brackets. Spherical caps and the main flange have been removed from the total mass.

Although we recognize that the pitch system is of great importance, it is not designed here, and its mass is estimated using a simple regression fit:

$$m_{ps} = 0.75 \left(0.22 * m_{bl} * B + \frac{12.6 * BRFM * \rho}{X_y} \right),$$
(5)

where m_{ps} is the mass of the pitch system, m_{bl} is the blade mass, which during the design of the drivetrain was assumed equal to 82.5 t, B is the number of blades equal to 3, $BRFM$ is the rated blade root flapwise moment of 172 MN m, ρ is the steel density of 7,850 kg m^{-3}, and X_y is maximum failure stress of 345 MPa. The resulting mass equals 78 t. Future work should focus on including detailed design models for pitch bearings and actuators because these components are increasingly critical for the production and operation of wind turbines of this size.

The total mass of the hub system sums to 120 t, its center of mass is located 3.5 m upwind of the main hub flange along the shaft axis, and the total mass moments of inertia are estimated to be 1.9E+6 kg m^2 around the rotor axis and 1.2E+6 kg m^2 in the two off-axis directions.

3.2 Generator

The generator for the 22 MW RWT is a direct-drive radial flux permanent-magnet synchronous generator; Figure 28a depicts a cross-sectional diagram. The generator has an outer rotor with interior permanent magnets in a V-shaped configuration for flux focusing, as shown in Figure 28b, and the stator has semi-closed slots with a double-layer fractional-slot concentrated winding. This outer rotor layout, with its simple and robust generator structure, facilitates easier manufacturing because the interior magnets are well-protected during assembly, and the stator's short end windings allow for a more compact design (compared to surface-mounted magnets). Moreover, the interior permanent magnets are less susceptible to permanent demagnetization.

The generator design optimization was carried out in three stages. First, the 22 MW generator was optimized by minimizing the generator's active material costs, subject to the specified electromagnetic and thermal performance constraints. This was done using GeneratorSE 2.0, which is built around the FEMM model [31, 32]. The second step refined the design with a coupled electromagnetic and steady-state thermal design using the commercial finite element analysis software Altair FLUX [33] and the optimization software ALTAIR Hyperstudy [34] to estimate eddy current losses and verify potential demagnetization from
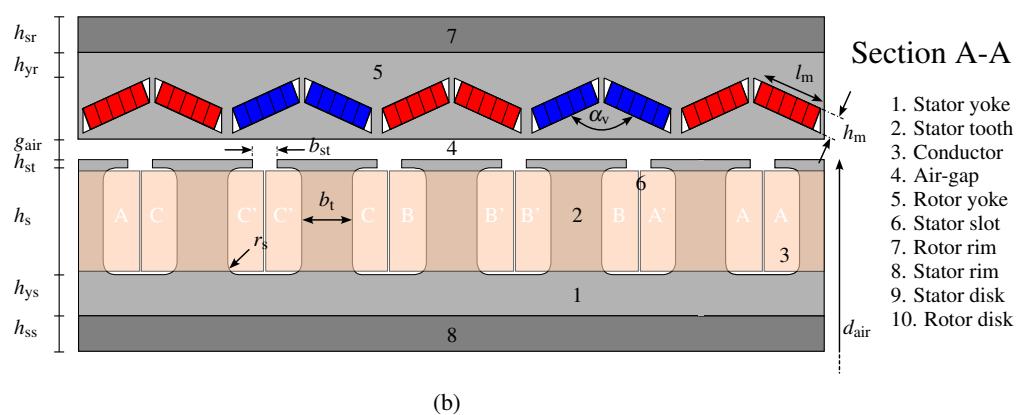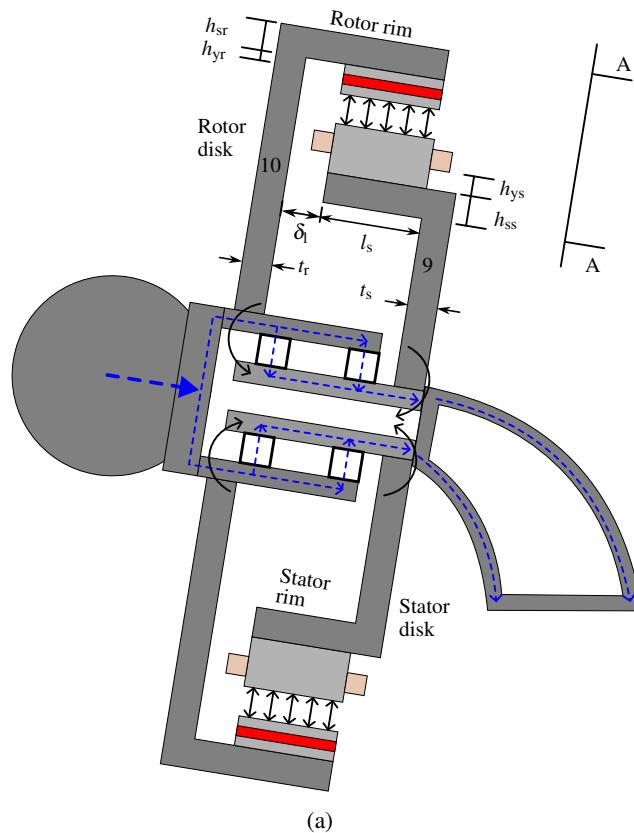
Figure 28: (a) Support structure and (b) V-shaped interior permanent magnets of the 22 MW generator design.

a short circuit. The third and last step included a design optimization of the support structure using a static analysis with the commercial software packages ANSYS Mechanical and ANSYS Workbench.

Some key modeling assumptions that guided the design optimizations include:

- The magnets used in the rotor are N45-SH neodymium (NdFeB) magnets. This magnet grade has a remnant flux density of $B_r = 1.35$ tesla (T) and a relative permeability of $\mu = 1.05$. The maximum operating temperature for these N45-SH magnets is 150 °C.
- To minimize eddy current losses in the magnets, the magnets are segmented in the radial and axial direction. The radial segmentation of the magnets can be seen in Figure 28b.
- Only a 2D modeling approach was adopted for the electromagnetic design, so contributions from end-effects are not accounted for.
- A 12–10 slot–pole combination with a fundamental winding factor of $k_w = 0.933$ was chosen for the base winding.
- A forced air cooling system is assumed for the generator with a maximum thermal convection coefficient of 500 $\text{W m}^{-2}\text{K}$. However, we did not conduct a detailed design of this cooling system, and the required cooling power was not considered a part of the generator efficiency calculations.
- Similar to the previous IEA 15 MW RWT, single-sided disc-type support structures are assumed to hold the electromagnetically active materials to greatly simplify the assembly.
- The air-gap length of the generator is assumed to be 7 mm. The air-gap is allowed to deflect by up to 20% of this distance, with both the iron yoke and the support structure contributing to the deformation. The magnets were assumed to be rigid. It is assumed that the hub loads from the blades are transmitted through the shaft, bearings, and turret assembly.

3.2.1 Electromagnetic and Thermal Performance

The electromagnetic design optimization of the generator sought to minimize the active material cost, C_{Gen}, which is given by

$$
\begin{aligned}
C_{\text{Gen}} &= M_{\text{PM}} \cdot C_{\text{PM}} + M_{\text{Cu}} \cdot C_{\text{Cu}} + (M_{\text{Fe-stator}} + M_{\text{Fe-rotor}}) \cdot C_{\text{Fe}} \\
&= M_{\text{PM}} \cdot 66.72 + M_{\text{Cu}} \cdot 7.3 + (M_{\text{Fe-stator}} + M_{\text{Fe-rotor}}) \cdot 1.56,
\end{aligned}
\tag{6}
$$

where M_x denotes the active mass of a specific material, and C_x denotes the specific cost in dollars per kilogram of that material. (NdFeB is the permanent magnet material, Cu is copper, and Fe is electric steel laminations.) The optimization for minimum active material cost is iterated with the best integer slot–pole count.

The optimized design features an air-gap diameter of 9.524 m and an axial stack length of 2.431 m. The final slot–pole count is 144–120. The total active material mass is 147.9 t, split between 25.2 t of magnet material, 17.1 t of copper, and 105.6 t for the rotor and stator laminations. The generator efficiency at rated load is 95.4% and is calculated by

$$
\eta = \frac{P_{\text{out}}}{P_{\text{out}} + P_{\text{Cu}} + P_{\text{Fe}} + P_{\text{PM}} + P_{\text{add}}},
\tag{7}
$$

where P_{Cu} is the copper losses in the stator winding (including the end-winding length), P_{Fe} is the iron losses in the rotor and stator laminations, P_{PM} is the magnet eddy current losses, and P_{add} is the additional rotational losses in the generator. The generator's power factor at rated load is 0.748, and is deemed acceptable for generators at this power rating. The root-mean-square (RMS) terminal voltage is 3.07 kV.

The nominal current in the windings at rated load translates to a current density of 5.1 A mm^{-2}, which is consistent with a forced air cooling system. Furthermore, the results from the thermal analysis predict that the steady-state temperature of the permanent magnets during rated operation will not exceed 90 °C, and the temperature of the windings is also below the thermal rating of the insulation. Throughout the analysis the ambient temperature was taken as 40 °C. As part of the final design's performance evaluation, a three-phase symmetrical short-circuit fault was simulated to determine the minimum remnant flux density of the magnets during this condition. The results indicated that the magnet area with a remnant flux density below the knee point is negligible.

The results from the 22 MW generator's drive-cycle analysis are shown in Figure 29. In Figure 29, the input power from the turbine, P_{in}, the output power at the generator terminals, P_{out}, and the corresponding generator efficiency, η, are plotted for each rotational speed in the operating range of the turbine.
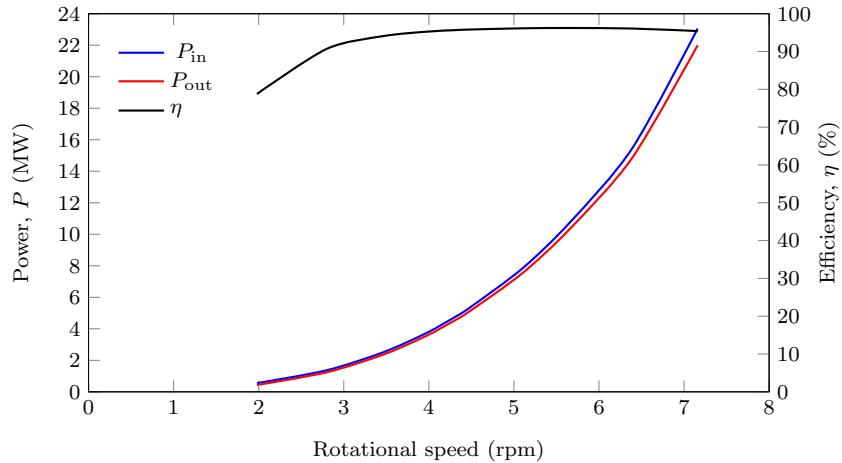
Figure 29: Drive-cycle analysis of the 22 MW generator.

3.2.2 Structural Design

The support structure was analogously optimized to minimize structural mass and to comply with the maximum allowed deflection in the air gap. For the static structural analysis, the normal component of the Maxwell stresses acting on the rotor and stator and the generator's shear stress were calculated using GeneratorSE 2.0. These loads were then applied to the generator structure as shown in Figure 30, where q is the normal stress, σ is the shear stress, and g is the gravity load.

The final structural design showed a maximum air-gap deflection of 17%, with the structural mass of the generator totaling 357.09 t, which is almost 70% of the total generator mass. The structural mass is split between 163.88 t for the stator and 193.21 t for the rotor. The torsional and axial deflection in the rotor and stator were also calculated, but these were insignificant compared to the air-gap deflection.
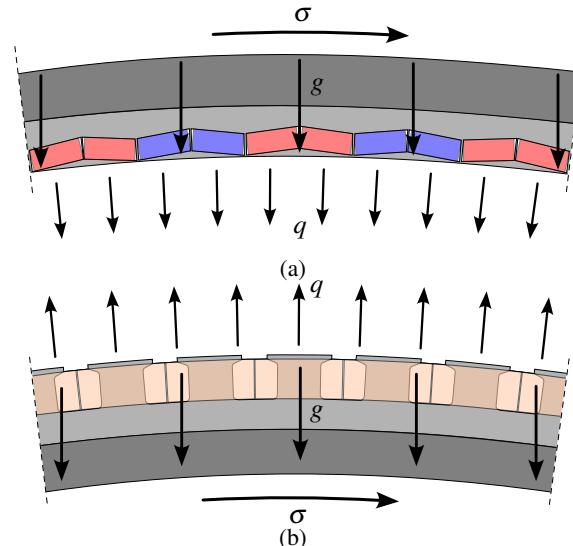
Figure 30: Illustrations of the loads acting on the generator's (a) rotor and (b) stator.

3.2.3 Final Design

The design and performance parameters of the optimized 22 MW generator are given in Table 9.

Table 9: Electromagnetic and structural design of the 22 MW direct-drive generator

Symbol	Description	Value	Units
P_r	Rated power at generator terminals	22	MW
ω_r	Rated speed	0.75	$\mathrm{rad\,s^{-1}}$
f_e	Electrical frequency	7.162	Hz
T_r	Rated torque	30.56	MN m
	Electromagnetic Design		
g_{air}	Air-gap length	7	mm
d_o	Outer diameter of generator's rotor yoke	9.759	m
d_{air}	Air-gap diameter	9.524	m
l_s	Axial length of the stack	2.431	m
h_{yr}	Rotor yoke height	50.0	mm
h_{ys}	Stator yoke height	69.0	mm
h_m	Magnet height	50.3	mm
l_m	Magnet width	112.9	mm
σ_m	Magnet pitch to pole pitch ratio	0.98	-
α_v	V-angle of magnet pole	164.8	deg
h_s	Slot height	91.4	mm
b_t	Tooth width	102.0	mm
h_{st}	Slot tooth height	10.0	mm
r_s	Slot edge radius	10.0	mm
b_{st}	Slot tooth opening width	57.0	mm
C_{fill}	Slot copper fill factor	0.55	-
V	RMS phase voltage	3,065.4	V
I	Nominal winding current (RMS)	3,182.9	A
R_s	Stator winding resistance per phase	0.028	Ω
N_s	Stator winding turns per coil	4.0	-
$\hat{B}_g$	Maximum air-gap flux density	1.57	T
J_s	Winding current density	5.1	$\mathrm{A\,mm^{-2}}$
A_1	Specific current loading	122.6	$\mathrm{kA\,m^{-1}}$
η	Efficiency at full load	95.4	%
P_{Cu}	Copper losses at full load	860.1	kW
P_{Fe}	Iron core losses at full load	138.3	kW
P_{PM}	Magnet losses at full load	29.1	kW
PF	Power factor at full load	0.748	-
M_{Fe}	Iron lamination mass	105.6	t
M_{Cu}	Copper mass	17.1	t
M_{PM}	Magnet mass	25.2	t
M_{Active}	Active mass	147.9	t
C_{Gen}	Active material cost	1,969,913	$
	Structural Design		
h_{ss}	Stator rim height	124	mm
t_s	Stator disk thickness	200	mm
h_{sr}	Rotor rim height	75	mm
t_r	Rotor disk thickness	266	mm
M_{SStru}	Total stator structural steel mass	163.88	t
M_{RStru}	Total rotor structural steel mass	193.21	t
M_{Gen}	Estimated total generator mass	504.93	t

3.3 Main Shaft, Bearings, Turret, and Bedplate

The design process of the main shaft, bearings, turret, and bedplate followed the same process adopted during the design of the 15 MW RWT. A depiction of these components is shown in Figure 31, with key parameters and dimensions listed in Table 10. The main shaft has a hollow cylindrical cross section with a constant wall thickness and a tilt angle of $6°$. The main shaft, along with the rotor, is supported by two main bearings. Both these main bearings have rotating outer raceways and fixed inner raceways. The inner raceways and bearing housing are accommodated by a turret held by the bedplate. The entire weight of the turbine rotor, generator rotor, and hub loads is transmitted by the main shaft to the turret via the bearings.

(a)

(b)
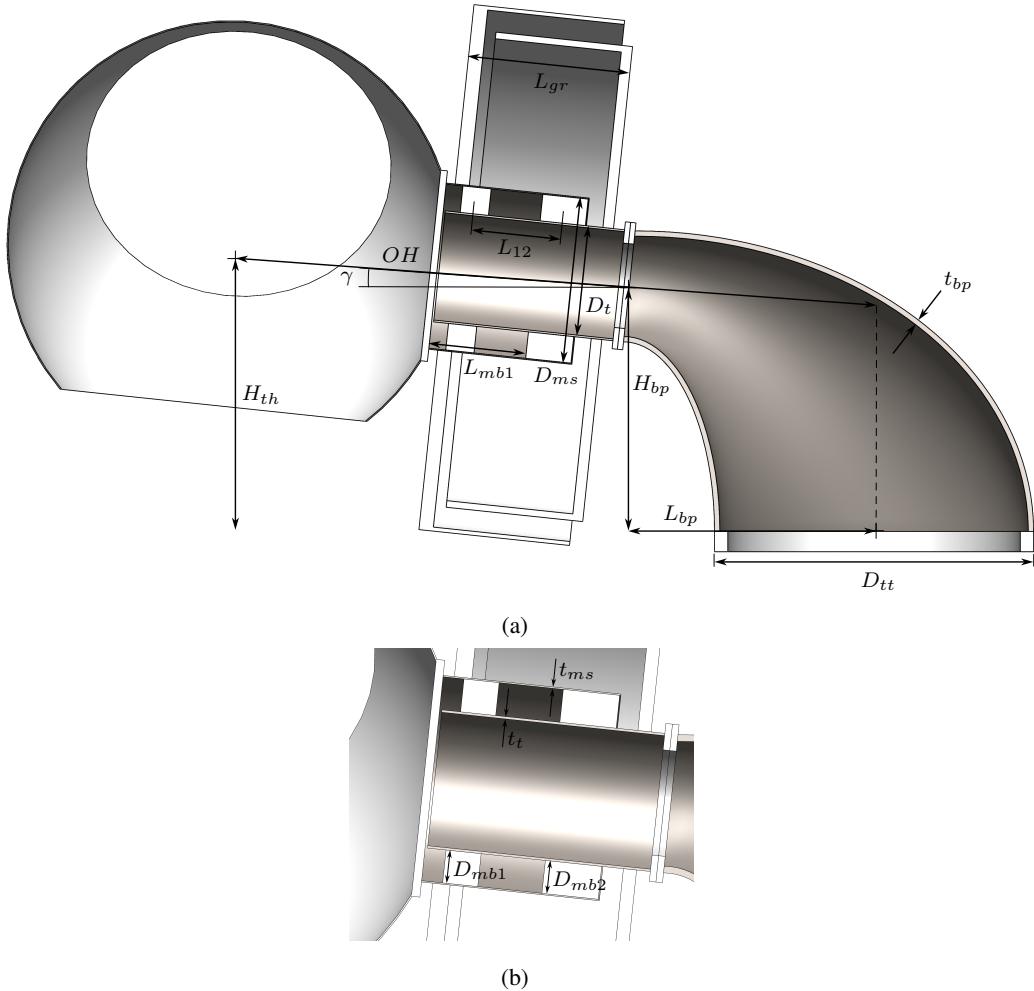
Figure 31: CAD illustration of the drivetrain; dimensions are documented in Table 10.

The inner diameter of the main shaft was designed with sufficient clearance for the nacelle turret and the main bearings. The thickness of the shaft was determined by ensuring a safe load path from the rotor while limiting the maximum deflection at the generator. It is assumed that the entire thrust load is transmitted by the main shaft to the upwind main bearing.

The turret is also modeled with a hollow cylindrical cross section with a constant wall thickness cantilevered from the bedplate. The inner diameter was constrained to 2 m to provide ample clearance for technician access. The thickness of the turret cylinder was determined by computing the reactions from the main bearings while limiting the maximum radial deflections at the interface with the generator rotor and stator. It is assumed that the turret carries all of the thrust imparted by the upwind main bearing, the moments from the transverse forces, and the torque.

The paired set of bearings consists of a fixed upwind bearing and a floating downwind bearing. A tapered double-outer configuration was chosen for the locating bearing (compact aligning roller bearing [CARB])

Table 10: Main dimensions of the drivetrain used in sizing

Symbol	Description	Value	Units
γ	Shaft tilt angle	6	deg
OH	Overhang	14.0	m
H_{th}	Vertical distance between tower top and hub center	5.614	m
D_{tt}	Diameter of tower top	6.0	m
L_{12}	Distance between upwind and downwind bearings	0.87	m
L_{mb1}	Distance of upwind bearing	1.83	m
L_{gr}	Length of the generator (stack width)	3.05	m
D_{ms}	Diameter of the main shaft	3.1	m
t_{ms}	Wall thickness of the main shaft	20	mm
D_t	Outer diameter of the turret	2.1	m
t_t	Wall thickness of the turret	35	mm
t_{bp}	Wall thickness of the bedplate	100	mm
L_{bp}	Length of the bedplate	4.6	m
H_{bp}	Height of the bedplate	4.6	m
D_{mb1}	Diameter of upwind bearing	0.48	m
D_{mb2}	Diameter of downwind bearing	0.48	m

and a spherical roller bearing (SRB) for the nonlocating bearing. The chosen bearing solutions were based on recommendations found in Smith [35], with a basic lifetime estimation for ultimate loads, as described in the DNV guidelines. Rated loads were used to determine the reactions at the main bearings. The upwind bearing was assumed to carry all axial loads and moments, whereas both the upwind and downwind bearings share the radial forces. These forces were directly transmitted to the turret and from there to the bedplate and tower. Because the downwind bearing carries smaller loads, we propose a bearing with a lower load rating.

Lastly, the bedplate is a hollow, elliptically curved, cantilever beam with circular cross sections. The bedplate has a smaller cross section that interfaces with the bedplate flange and a larger cross section that interfaces with the yaw bearing at the tower top. The thickness of the circular ring elements is optimized to constrain the cumulative stresses from bending, torsion, shear forces, and axial loads to 200 MPa. The total end deflection is an input into the turret design for an accurate air-gap deflection estimate. The driving load case is taken from an extreme aerodynamic gust at rated conditions.

3.4 Yaw System

Like the pitch system, the yaw system is only sized using a regression fit and not through a bottom-up design model. The mass of the yaw system is assumed to be the simple sum of the mass of a friction plate and of 18 motors with a mass of 190 kg each. The mass of the friction plate is equal to 25,320 kg and is estimated based on tower-top diameter and wind turbine rotor diameter. The mass of the yaw system is estimated to be 28,741 kg, the center of mass is assumed to sit at the tower-top center point, and no rotational inertia is assumed.

3.5 Equivalent Rigid-Body Properties of the Nacelle

A number of aeroelastic models use inputs of equivalent rigid-body properties for the whole nacelle assembly, instead of geometrical dimensions of the individual components. These properties are provided in Table 11.

The aerodynamics of the nacelle are modelled with a simple drag coefficient equal to 0.5. The outer dimensions of the nacelle are estimated equal to 18 m in length, 11 m in width, and 11 m in height.

Table 11: Centers of mass, lumped masses and moments of inertia for the nacelle assembly estimated by WISDEM and used in the aeroelastic models OpenFAST and HAWC2. The centers of mass are defined with respect to the tower-top (TT) coordinate system, whereas the mass moments of inertia are defined with respect to coordinate systems whose origins are defined at the center of mass of each component, and the axes are oriented as the TT coordinate system. The TT coordinate system is located at the top of the tower, with x pointing in the main wind direction, y pointing to the side, and z pointing vertically up.

Name	X_{TT} [m]	Z_{TT} [m]	Mass [t]	I_{xx} [kg m^2]	I_{yy} [kg m^2]	I_{zz} [kg m^2]
Hub system	3.54	0.0	120.0	1.9E+6	1.2E+6	1.2E+6
Shaft	3.87	0.0	4.1	9.7E+3	7.4E+3	7.4E+3
CARB	3.39	-	42.6	5.5E+4	3.0E+4	3.0E+4
SRB	2.52	-	12.4	1.6E+4	8.7E+3	8.7E+3
Inner generator stator	2.78	-	254.0	3.1E+3	1.8E+6	1.8E+6
Outer generator rotor	2.78	-	254.0	3.1E+3	1.8E+6	1.8E+6
Generator	2.78	-	508.0	6.2E+6	3.5E+6	3.5E+6
Turret	1.69	0.0	6.0	6.4E+3	9.0E+3	9.0E+3
Bedplate	−1.20	2.48	75.1	8.8E+5	1.1E+6	6.2E+5
Brake	4.31	0.0	39.2	4.0E+4	2.0E+4	2.0E+4
Converter	0.0	2.1	17.4	5.3E+4	5.3E+4	5.3E+4
Transformer	0.0	2.1	44.0	1.3E+5	1.3E+5	1.3E+5
HVAC	2.78	0.0	12.8	1.8E+5	8.9E+4	8.9E+4
Platform	0.0	0.0	41.4	5.0E+5	5.0E+5	1.0E+6
Cover	−0.23	5.45	17.8	1.3E+3	0.9E+3	0.9E+3
Yaw system	0.0	0.0	37.5	0.0	0.0	0.0
Nacelle no hub/yaw	5.85	4.26	821.2	1.25E+07	1.62E+07	1.68E+07
Nacelle no hub/yaw TT				2.62E+07	5.76E+07	4.28E+07
Rotor-nacelle assembly TT	8.65	4.62	1,215.6	7.42E+08	5.14E+08	4.90E+08

4 Tower and Monopile

The 22 MW RWT has a hub height of 170 m, with a 5.614 m vertical distance between the rotor apex and tower top. The tower is assumed to start 15 m above mean sea level and its length is therefore 149.386 m. The monopile is designed for a water depth of 34 m and its length in the seabed is 45 m, giving a total length of 94 m to reach the tower base. The assembly also includes a transition piece, which is modeled as a simple point mass of 100 t and is located between tower and monopile 15 m above mean sea level. The hub height of 170 m leaves a clearance of 30 m between mean sea level and blade tip (not including loaded deflections). This clearance is computed as hub height minus the rotor radius times the cosine of hub precone and shaft tilt angles.

4.1 Design Process

The distributions of outer diameter and wall thickness along the tower and monopile were ascertained via a design optimization in WISDEM that sought to minimize the combined support structure mass. The tower was modeled in 30 segments and the monopile in 10 segments. The diameter variation was bounded between 6 m at the tower top and a maximum dimension of 10 m. Both bounds were met in the final design. Optimization bounds were also applied to the wall thickness, but were not active in the final design. Constraints that guided the optimization problem include:

- Maximum stress along tower and monopile could not exceed the yield strength of steel of 345 MPa. PSFs of 1.35 for loads, 1.3 for materials, and 1.0 for consequence of failure were assumed.
- Global and shell buckling as specified by the DNVGL standards DNV-RP-C202 "Buckling strength of shells."
- Diameter-to-thickness ratios between 80 and 160 to ensure that manufacturability requirements are met.
- Monotonically decreasing wall thickness moving upwards to avoid unrealistic variations in thickness.
- A minimum natural frequency of the overall fixed-bottom turbine system of 0.15 Hz. The values were chosen to provide sufficient margin to both wave excitation, which for a generic U.S. East Coast site is between 0.1 and 0.13 Hz, and to the first rotor harmonic (1P) at rated conditions, which for a rotor speed of 7.1 rpm is equal to 0.12 Hz. Note that soil is assumed stiff.
- Tower-to-monopile coupling to ensure that the top of the monopile and the bottom of the tower have the same diameter.

Tower and monopile are made of the same steel, the properties of which are listed in Table 12.

Table 12: Mechanical properties of the steel adopted in the tower and in the monopile

Property	Value	Property	Value
Density	7,850 kg m^{-3}	Young's modulus	200 GPa
Shear stiffness	79.3 GPa	Poisson's ratio	0.265
Tensile strength	450 MPa	Compressive strength	450 MPa
Yield strength	345 MPa	Fatigue slope	3

The loading on tower and monopile was applied at tower top. Forces were 5.4 MN, 0.09 MN, and -8.9 MN in x, y, and z directions, respectively. Moments in the x, y, and z directions were -1.6 MN m, -13.3 MN m, and 10.8 MN m, respectively. Quantities are expressed in the tower-top coordinate system where x points downwind, y points sideways, and z points upwards. The equivalent properties of the rotor-nacelle assembly are listed in the last row of Table 11. The total mass of the rotor-nacelle assembly is 1,215.6 t. Note that in contrast to the 15 MW RWT, no outfitting factor was included in the design. The outfitting factor is useful to artificially augment the mass of the tower to account for auxiliary systems such as stairs, elevators, platform, bolt connections, etc. However, these masses are not load-bearing, so they were excluded in this model.

4.2 Structural Design

This section describes the final design of tower and monopile. The final tower mass is 1,574 t, and the final monopile mass is 2,097 t. Outer diameter and wall thickness distributions along the height are reported in Figure 32. The design is driven by the constraint on global buckling, which is active throughout the height of the tower and monopile, except for the sections located inside the seabed. The natural frequencies of the full assembly estimated by WISDEM, including the rotor and the nacelle, are reported in Table 13.
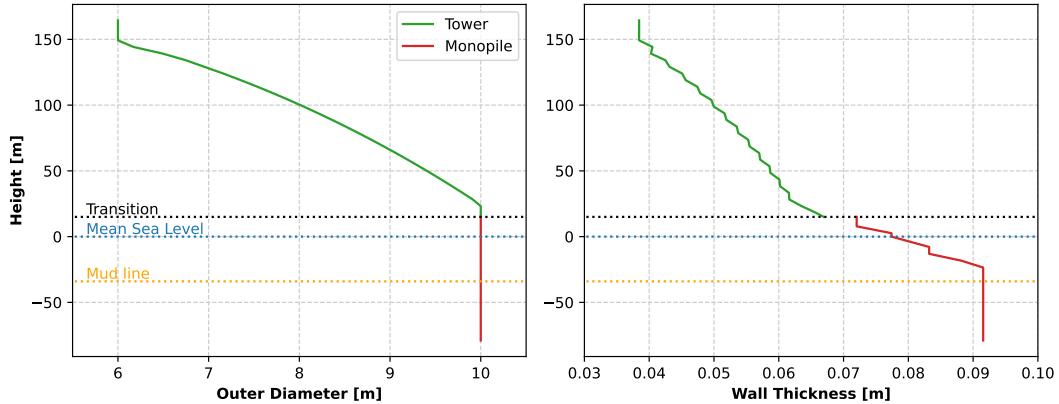

Figure 32: Outer diameter and wall thickness distributions of tower and monopile.

Table 13: Fore-aft, side-side, and torsional natural frequencies of the turbine clamped at tower base and of the turbine mounted on the monopile. Natural frequencies are computed in WISDEM and include the rotor-nacelle assembly.

Frequency [Hz]	First	Second	Third
Turbine clamped at tower base			
Fore-aft	0.22	1.01	2.49
Side-side	0.22	0.88	2.42
Torsion	5.2	-	-
Turbine clamped at monopile base			
Fore-aft	0.16	0.82	1.70
Side-side	0.16	0.74	1.61
Torsion	4.72	-	-

The stiffness and mass distributions along the tower and monopile are available in the supplementary files in the project repository.

4.3 Structural Damping

For aeroelastic modeling, the structural damping of the tower and monopile is also needed. The input values are tuned so that first fore-aft and side-side modes of the isolated components (tower and monopile taken individually, excluding the tower-top mass) have a damping ratio ζ equal to 0.5%. The value is possibly low and conservative, although large variations are observed in other aeroelastic models. When the components are assembled in the solver HAWC2, the structural damping of the first fore-aft and side-side modes of full system is equal to 0.092%. The second modes are at 0.54% and 0.52%, respectively.

In OpenFAST, the structural damping of the tower is set as an input in its module ElastoDyn, whereas the structural damping of the monopile is modeled through Rayleigh damping in the module SubDyn. Only the stiffness proportional term is set here following this equation:

$$\beta = \zeta/(\pi \cdot f) \tag{8}$$

where ζ is for the full system and is equal to 0.092%, and f is the natural frequency of the first fore-aft mode of the full system, equal to 0.16 Hz, as listed in Table 13. The resulting β is equal to 0.00183. For the tower, which is modeled in the ElastoDyn module of OpenFAST, structural damping of the first fore-aft and side-side modes is set as

$$\zeta_i = \zeta_t \cdot f_u / f_c \tag{9}$$

where ζ_i is the input value to ElastoDyn, ζ_t is the target damping ratio equal to 0.092%, f_u is the frequency of the uncoupled tower (isolated tower, no monopile and no tower top mass) equal to 0.583 Hz, and finally f_c is the frequency of the full coupled system (full rotor nacelle assembly, tower, and monopile) equal to 0.16 Hz. The resulting ζ_i is equal to 0.33%. For the values of ζ of the second modes, the values were tuned manually to achieve target values of 0.517% and 0.537% for second side-side and second fore-aft modes of the full system, respectively.

Note that the values of ζ of the isolated tower in ElastoDyn were also applied to the floating tower. These values will need to be reviewed, and possibly adjusted, in future work. Also, when modeling the turbine system as a land based machine, i.e. without the monopile, the tuning of the tower ζ in ElastoDyn will no longer match the values predicted by HAWC2. In this case, the user should change the value of ζ of 0.33% to 0.5% for the first modes and 2.1678% and 2.1698% for the second modes. Note also that when modeling an isolated tower, ElastoDyn requires the user to update the mode shapes.

4.4   Aerodynamics and Hydrodynamics

The aerodynamic loading on the tower is modeled adopting a constant drag coefficient of 0.5. The hydro-dynamics of the monopile are modeled by adopting drag, added mass, and pressure coefficients equal to 1.0. The effective mass coefficient, also referred to as the inertia coefficient, is the sum of added mass and pressure coefficients and is therefore equal to 2.0. The monopile is modeled as filled with seawater.

5 Semisubmersible Floating Platform

5.1 Tools and Design Basis

The goal when designing a floating platform for the IEA 22 MW RWT was to mimic the 15 MW VolturnUS-S design [36] for this larger turbine and use tools easily and openly available to the wind energy community. The design is intended to be used as a baseline for future floating platform designers in terms of dynamic performance and cost modeling for large-scale floating offshore wind turbines. The resulting design is thought to be representative of a plausible in-water system in terms of its dynamic behavior. Our design process focused on the floater geometry and hydrodynamics in this initial design. We did not consider manufacturing constraints, structural analysis, or a detailed mooring design, though we have provided a starting point for those avenues of future work.

We used the WEIS toolset to design a steel semisubmersible platform similar to the geometry of the VolturnUS-S platform. Within WEIS, WISDEM is used to preprocess input geometry comprising a set of members (e.g., columns and pontoons) and joints (the endpoints of those members). WISDEM is also used to calculate static constraints, like whether ballast chambers are adequately sized and, if in extreme conditions, the draft and freeboard of all columns avoid leaving the water or entering the water, respectively. The frequency domain model RAFT [37] was used to calculate steady-state offsets and a frequency domain response of the floating offshore wind turbine motion. Given environmental wind and wave conditions, the standard deviations, maxima, and minima can be estimated in RAFT for several turbine outputs. Using the preprocessed geometry, WEIS generates an OpenFAST model to verify the dynamics in RAFT, and ROSCO is used to control the turbine. We used a gravity constant of 9.80665 m/s^2 and water density of 1025 kg-m^2 in all the modeling software.

This platform design maintains the same semisubmersible architecture used in the VolturnUS-S platform, with three outer columns and a center main column. The geometry is shown in Figure 33. Other system properties are shown in Table 14. The turbine is simulated in design load cases (DLCs) 1.1, 1.6, and 6.1 from the International Electrotechnical Commission Standards [38, 39]. These load cases prescribe normal turbulence and sea state (DLC 1.1), normal turbulence and severe sea state (1.6), and 50-year extreme wind and sea state (6.1). The metocean conditions are representative of the Gulf of Maine. In contrast to the VolturnUS-S platform, only water ballast is used in this semisubmersible platform; this was done to simplify the design procedure. Since structural analysis was not performed in this version of the design, we simply increased the size of the lower pontoons to 10 m. The wall thickness of the outer columns was set at 5 cm, and the lower pontoons have a thickness of 4 cm. We should note that there is a structural discontinuity at the base of the tower. We used the same tower as the fixed-bottom turbine, which has a tower base of 10 m and a fixed center column diameter of 12 m. A floating-specific tower and structural analysis can be evaluated in future work.

Table 14: General system properties

Property	Unit	Value
Platform type	-	Semisubmersible
Freeboard	m	15
Draft	m	25
Total system mass	t	23,984.1
Platform mass	t	21,165.6
Water depth	m	200.0
Mooring system	-	Three-line chain catenary

5.2 Design Optimization

The design variables, constraints, and merit figures of the platform design optimization problem are shown in Table 15. We use an optimization solver to evaluate the trade-offs between the merit figure and constraints while inherently accounting for coupling between the design variables and the design objectives.
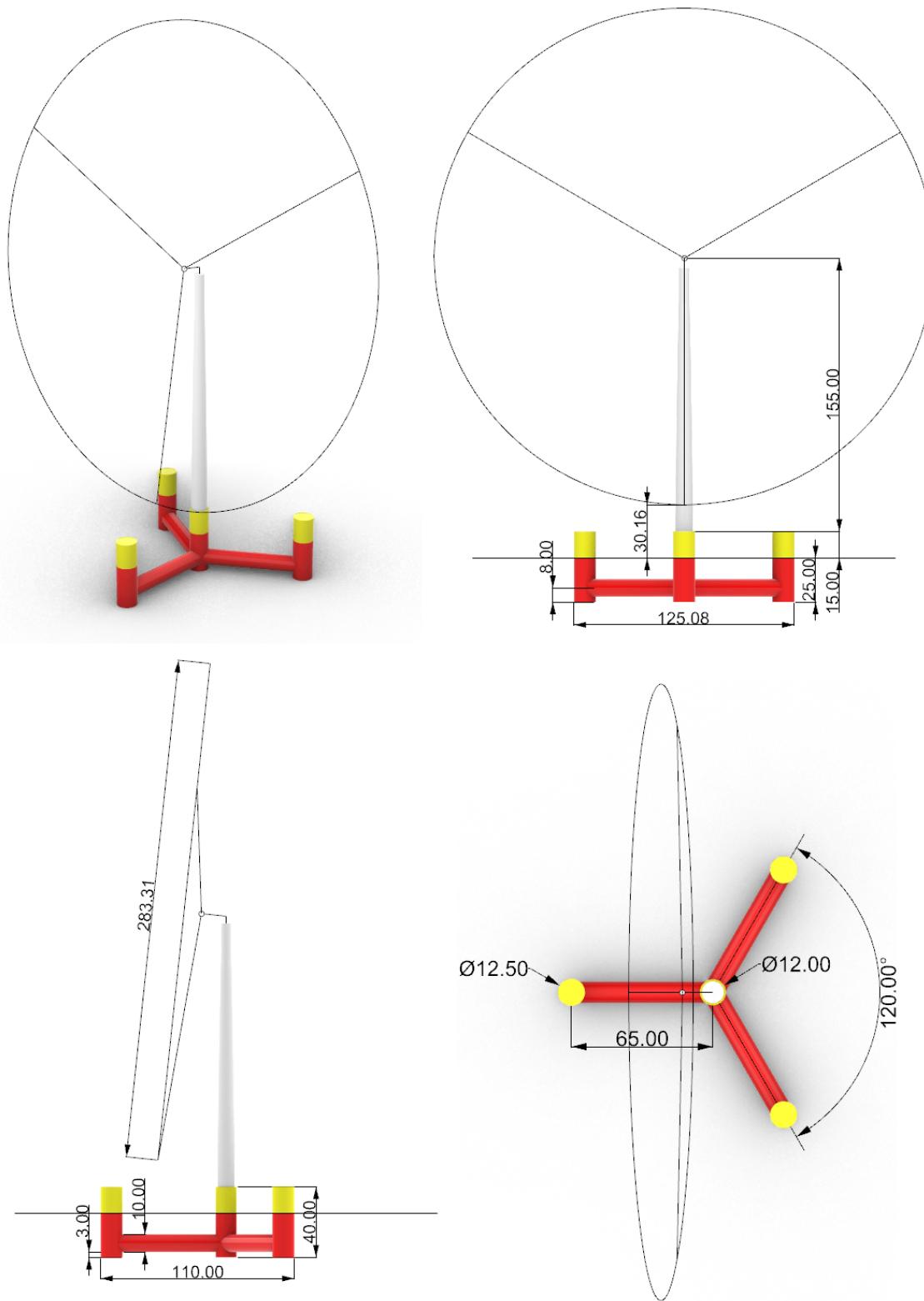
Figure 33: Designed dimensions of the IEA 22 MW RWT semisubmersible platform. All dimensions are in meters and degrees.

The column spacing is measured from the center of the center column to the center of the outer columns. The draft is relative to the waterline. The natural period constraints were placed to avoid excitation in severe sea states. Increasing the heave natural period led to infeasible designs. The survival heel angle is used to determine whether the columns leave the water or become completely submerged. The maximum

Table 15: Merit figure, design variables, and constraints for the platform design optimization

Merit Figure		Platform structural Mass
Design Variable	Lower Bound	Upper Bound
Column spacing	35 m	100 m
Draft	20 m	50 m
Outer column diameter	10 m	16 m
Constraint	Lower Bound	Upper Bound
Metacentric height	15 m	
Pitch period	20 s	80 s
Heave period	16 s	80 s
Survival heel		10 deg
Maximum platform pitch		5.5 deg
Maximum nacelle acceleration		2 m/s^2

and standard deviation (std.) of platform pitch constraints are evaluated as the maximum over all DLCs. The standard deviation of the platform pitch was selected to match the IEA 15 MW VolturnUS-S platform in the same DLCs. The resulting design is a product of the selected constraints and merit figure. The effect of various constraints on the design will be evaluated in future work.

5.3 Hydrodynamic Model Details

Key properties of the optimized semisubmersible platform shown in Figure 33 are provided in Table 16. The first-order potential-flow hydrodynamic properties of the optimized platform geometry were computed using the commercial boundary-element-method solver WAMIT [40]. The computation was performed with the higher-order panel method and a maximum panel size of approximately 2 m. Sum- and difference-frequency quadratic transfer functions for the second-order potential-flow wave excitation will be added in the future.

Table 16: Semisubmersible platform properties

Parameter	Unit	Value
Hull displaced volume	m^3	24,727.0
Hull steel mass	t	5,710.6
Water ballast mass	t	15,455.0
Freeboard	m	15
Draft	m	25
Vertical center of gravity from still water level (SWL)	m	-15.2
Vertical center of buoyancy from SWL	m	-14.8
Waterplane area	m^2	481
Roll inertia about center of gravity (CoG)	kg m^2	2.30E+10
Pitch inertia about CoG	kg m^2	2.30E+10
Yaw inertia about CoG	kg m^2	4.32E+10

The frequency-dependent added mass/moment of inertia and wave radiation damping coefficients are shown in Figure 34. The infinite-frequency added mass/moment of inertia is provided in Table 17.

The unit-amplitude wave excitation was computed for the full range of possible wave headings from $-180°$ to $+180°$ at $10°$ intervals. Figure 35 shows the unit-amplitude wave excitation in surge, heave, and pitch for a $0°$ wave heading. The wave excitation in all other directions is zero in this case due to port-starboard symmetry.

The hydrostatic stiffness matrix determined by WAMIT, with respect to the platform reference point (the

Table 17: Infinite-frequency added mass/moment of inertia matrix of the semisubmersible platform (kg, kg m, kg m^2)

	Surge	Sway	Heave	Roll	Pitch	Yaw
Surge	1.478E+7	0.00	0.00	0.00	−2.073E+8	0.00
Sway	0.00	1.478E+7	0.00	2.073E+8	0.00	0.00
Heave	0.00	0.00	1.524E+7	0.00	0.00	0.00
Roll	0.00	2.073E+8	0.00	1.463E+10	0.00	0.00
Pitch	−2.073E+8	0.00	0.00	0.00	1.462E+10	0.00
Yaw	0.00	0.00	0.00	0.00	0.00	4.808E+10

Table 18: Hydrostatic stiffness of the semisubmersible platform without contributions from self-weight

	Surge	Sway	Heave	Roll	Pitch	Yaw
Surge	0.00	0.00	0.00	0.00	0.00	0.00
Sway	0.00	0.00	0.00	0.00	0.00	0.00
Heave	0.00	0.00	4.84E+6 N m^{-1}	0.00	0.00	0.00
Roll	0.00	0.00	0.00	4.18E+9 N m rad^{-1}	0.00	0.00
Pitch	0.00	0.00	0.00	0.00	4.18E+9 N m rad^{-1}	0.00
Yaw	0.00	0.00	0.00	0.00	0.00	0.00

center of the waterplane area), is shown in Table 18. The contributions from self-weight are not included because they will be added separately by OpenFAST.

We have constructed two OpenFAST/HydroDyn models of the floating platform described in Table 16. One model exclusively uses strip-theory members with a Morison-equation-type load formulation. This model provides distributed hydrodynamic and hydrostatic loads over the entire floating structure and is more convenient when simulating a flexible platform to obtain the internal structural loads. For the transverse hydrodynamic load on the vertical columns, the added mass coefficient, C_a, and the pressure coefficient, C_p, are both set to unity. For the pontoons, we use $C_p = 1$ and a slightly increased C_a of 1.2 to better match the heave and pitch wave excitation from the potential-flow solution. The axial added mass and dynamic pressure coefficients for member end plates are both set to unity for all columns and pontoons. A transverse drag coefficient of $C_d = 0.6$ is used for all columns and pontoons. Finally, an axial drag coefficient of 4.0 is chosen for the bottom of the columns. The use of these coefficients is documented in Jonkman et al. [41].

The other model is based on potential-flow solutions augmented with strip-theory quadratic drag force. The same set of drag coefficients from the strip-theory model is adopted. This model is expected to be more accurate; however, the floating platform can only be modeled as rigid due to the lack of local hydrodynamic and hydrostatic load information.

Note that the drag coefficients used in either model were tentatively selected based on experience and were not tuned to high-fidelity computational fluid dynamics simulations or experiments. Calibration of the drag coefficients is left for future work.

Comparisons between the strip-theory-only model and the potential-flow model are shown in Figure 35 and Figure 36. Figure 35 shows the unit-amplitude wave excitation on the structure derived from OpenFAST simulations of a fixed platform in white-noise waves (0° wave heading). The vertical line indicates the wave frequency that leads to a wavelength equal to 5 times the outer column diameter. This is a generally accepted threshold for the applicability of the Morison equation [42]. Reasonable agreement between the two models is observed below this frequency. Beyond this frequency, the Morison equation overpredicts the wave excitation, especially in surge, and agreement between the two models cannot be expected.

Figure 36 compares the motion response amplitude operators (RAOs) derived from OpenFAST simulations of a moored platform in white-noise waves (0° wave heading). All degrees of freedom except those associated with the motion of the platform were disabled in the OpenFAST simulations. Note that Figure 36(a) and (c) use two different vertical scales for the low-frequency region ($f \leq 0.04$ Hz) and the typical wave-frequency region ($f > 0.04$ Hz) for clarity. Reasonable agreement between the strip-theory and potential-flow models is observed. Most importantly, both models predict consistent system resonance

(a) Surge, sway, and heave added mass

(b) Surge, sway, and heave damping

(c) Roll, pitch, and yaw added moment of inertia

(d) Roll, pitch, and yaw damping

(e) Surge-pitch and roll-sway coupling

(f) Surge-pitch and roll-sway coupling
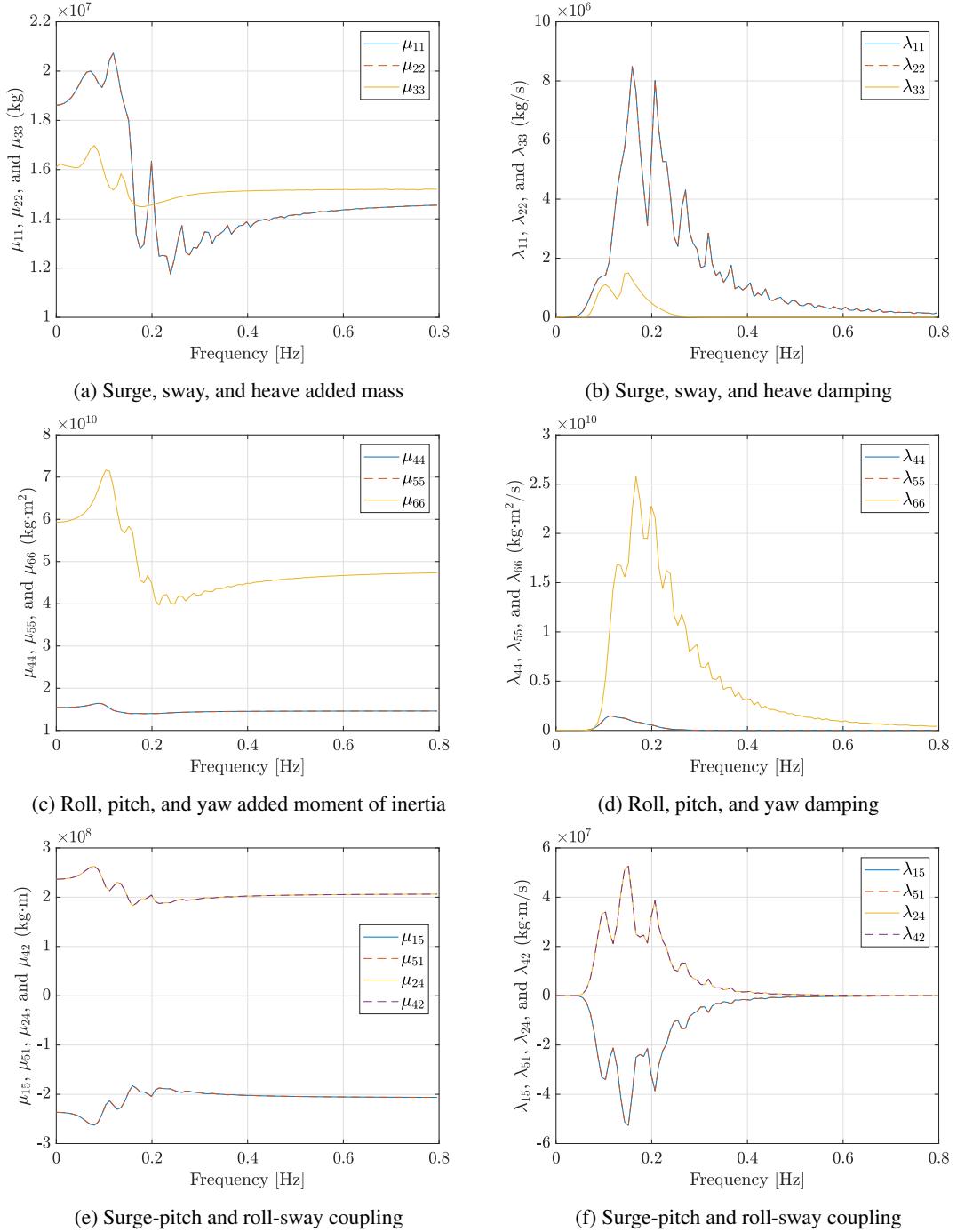
Figure 34: Potential-flow added mass/moment of inertia and wave-radiation damping coefficients evaluated by WAMIT. μ and λ are the entries of the added mass/moment of inertia and wave radiation damping matrices, respectively. The indices of the coefficients represent the surge, sway, heave, roll, pitch, and yaw degrees of freedom numbered 1 through 6 in that order.

frequencies in surge, heave, and pitch.

5.4 Mooring System

A three-line chain catenary mooring system was designed for this system, similar to the VolturnUS-S configuration. The mooring system properties are shown in Table 19. The coefficients, densities, stiffnesses,

(a) Surge force

(b) Heave force

(c) Pitch moment
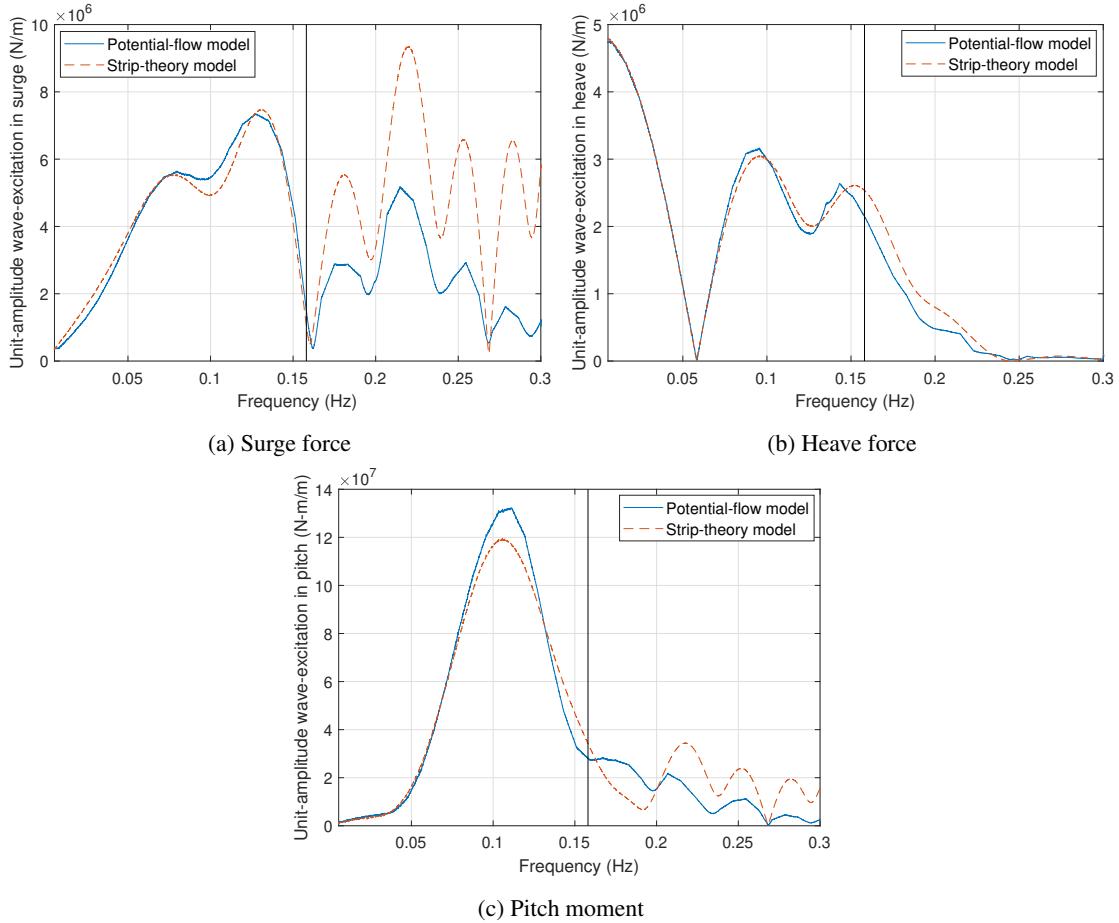
Figure 35: Comparison of unit-amplitude wave excitation in (a) surge, (b) heave, and (c) pitch obtained from the potential-flow model and the strip-theory model (0° wave heading).

and breaking strength are derived from the MoorPy tool [43]. The same line properties were used as in the VolturnUS-S design, but the unstretched line length was altered to maintain a similar maximum offset to the VolturnUS-S system. A diagram of the mooring system is shown in Figure 37.

Table 19: Mooring system properties

Property	Unit	Value
Mooring system type	-	Chain catenary
Line breaking strength	MN	103.8
Number of lines	-	3
Anchor depth	m	200.0
Fairlead depth	m	18.1
Anchor radial spacing	m	837.8
Nominal chain diameter	mm	400
Linear density	$kg\,m^{-1}$	3,184.0
Extensional stiffness	N	1.367E+10
Line unstretched length	m	837.0
Transverse drag coefficient	-	1.6
Transverse added mass coefficient	-	1.0
Tangential drag coefficient	-	0.1
Tangential added mass coefficient	-	0

(a) Surge RAO

(b) Heave RAO

(c) Pitch RAO
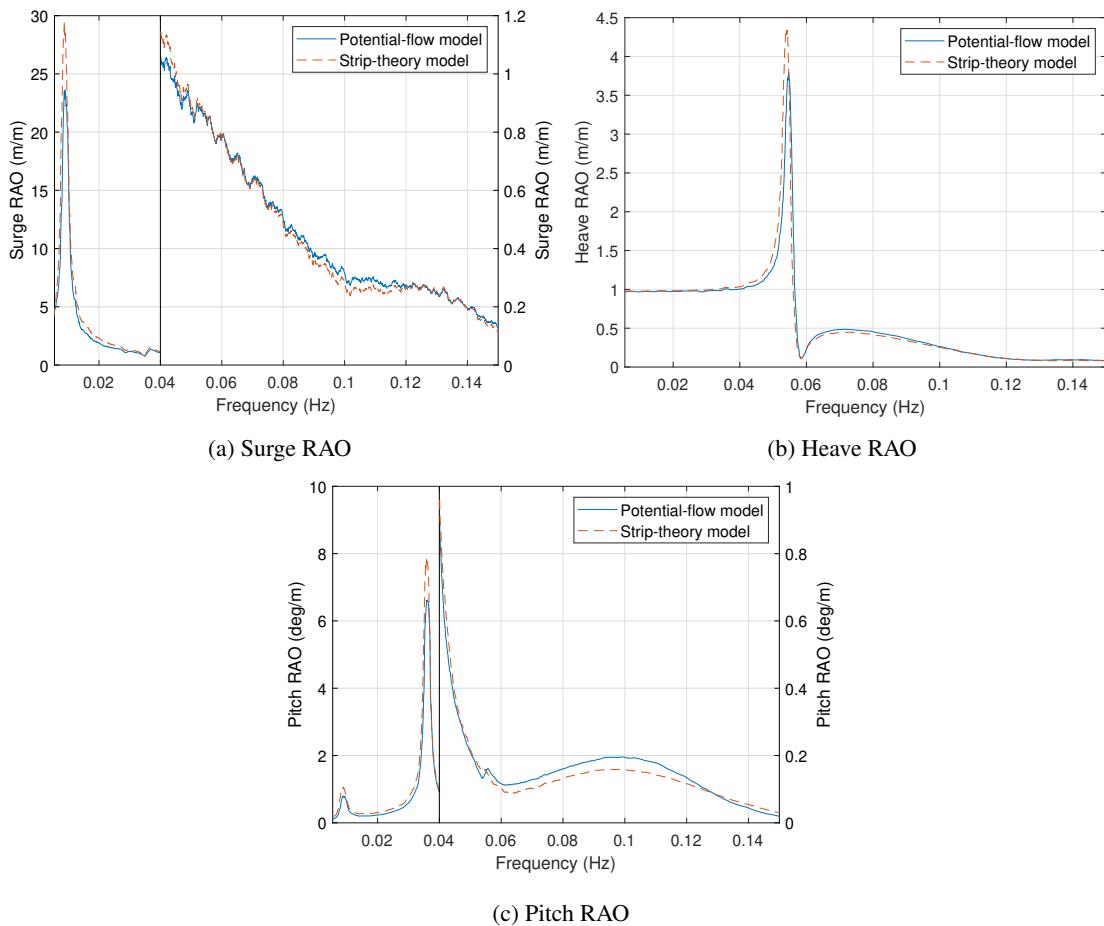
Figure 36: Comparison of platform motion response amplitude operators (RAOs) in (a) surge, (b) heave, and (c) pitch obtained from the potential-flow model and the strip-theory model (0° wave heading).
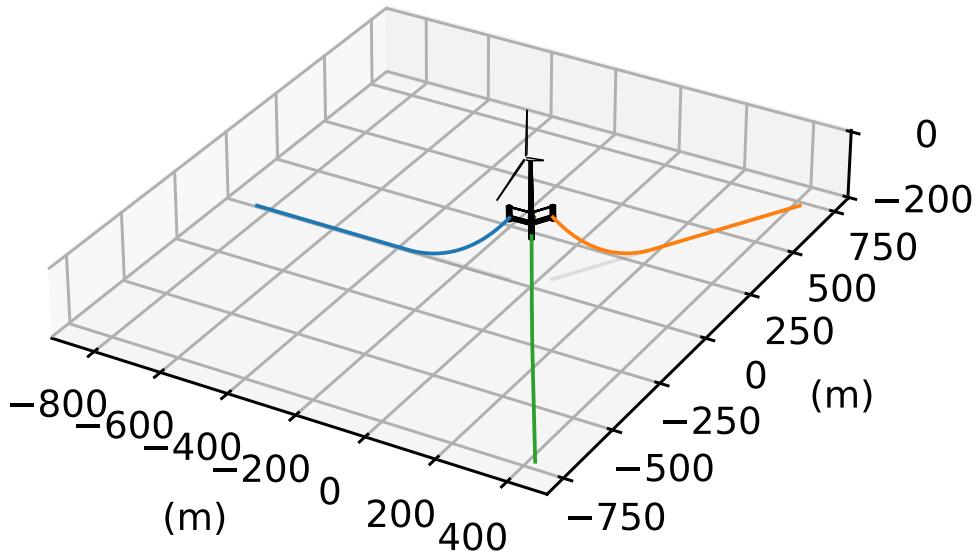

Figure 37: Mooring system for the IEA 22 MW RWT.

5.5 Floating Tower

At the time of this report's publishing, the same tower was used for both the floating and fixed-bottom configurations. Compared to the monopile tower, the natural frequency of the floating tower increases from 0.16 Hz to 0.22 Hz, making this a soft-stiff tower. A stiff-stiff tower would be prohibitively heavy for this floating turbine size. The 3P rotor harmonic at 4.4 rpm will excite the tower's natural frequency. This condition occurs around $7.1 \ \text{m s}^{-1}$. A tower resonance avoidance scheme should be able to avoid this rotor speed in future iterations of the design.

5.6 ROSCO Controller

For both the fixed-bottom and floating turbine models, we tuned an instance of the ROSCO v2.8.0 controller. We use a torque controller to track the optimal tip-speed ratio and rotor speed in below-rated operation. A minimum pitch versus wind speed lookup table is used to optimize the blade pitch angles at low wind speeds. These pitch angles were found to be optimal with the HAWC2 software. A low-pass filtered wind speed estimate is used as the wind speed signal.

During above-rated operation, the torque controller of the monopile system will use a constant power configuration, where the torque is varied to output a constant 22 MW. The floating controller will use a constant torque configuration, which improves platform stability but allows the power to vary more than the constant power configuration.

In both systems, a gain scheduled pitch controller is optimized to minimize the tower damage equivalent loads, with a constraint on the maximum generator speed, which is not allowed to exceed 20% of the rated generator speed. A set of 72 DLC 1.1 simulations from cut-in to cut-out wind speed were used to compute these measures for each design iteration. For the floating system, the gain and phase of the floating feedback control loop were also optimized.

A set point smoothing algorithm is used to bias the torque and pitch control generator speed set points so that only one is active during most times, while the other is saturated at the maximum torque or minimum pitch. In future work, we plan to add soft cut-out control for high wind speeds and frequency avoidance, so excitations from the 3P rotor speed on the soft-stiff floating tower can be reduced.

A comparison between the ROSCO controller with OpenFAST and the DTU Wind Energy controller with HAWC2 will be documented in future work. Both controllers have been developed with shared intentions: tracking generator speed similarly and limiting the maximum rotor thrust to the same value. Thus, the controllers should result in similar performance. The ROSCO controller follows the standard Bladed interface for controllers, so it can be used with any of the software packages modeling the IEA-22MW RWT using that interface.

6 Detailed Loads Evaluation

The 22 MW RWT model with the designed rotor and tower from Section 2 and Section 4 is first evaluated in the aeroelastic tool HAWCStab2 [28] in terms of aeroelastic steady-state performance and stability, where the controller parameters are also tuned. Subsequently, the model is set up in the time-domain aeroelastic tool HAWC2 [17] where first the controller performance is verified and then a design load basis (DLB) evaluation is performed for the evaluation of lifetime extreme and fatigue loads for the specified site conditions and a number of Design Load Cases (DLC).

Note that the results presented and discussed in the next subsections are also included in the GitHub repository, where results for different solvers will be uploaded when available.

6.1 HAWCStab2 Stability and Controller Tuning

In HAWCStab2 [28], the aeroelastic steady-state performance is verified using the designed operational rotor speed and pitch settings. The isolated blade and full turbine aeroelastic modal analysis is performed, where the first 20 aeroelastic frequencies and damping of the full system are verified and shown in Figure 38 and Figure 39. Figure 40 shows the damping within the 0–15% damping ratio area. It is shown that the lowest system frequency is located at 0.12 Hz, and all modes exhibit positive damping. The fore-aft and side-to-side modes are located around 0.12 Hz, and the first rotor modes (symmetric and whirling) are located around 0.3–0.6 Hz in below-rated conditions. The DTU Wind Energy controller (DTU-WEC) [44] parameters are tuned in HAWCStab using the pole placement method. With some iteration on the performance of the controller in the time domain in HAWC2, a closed-loop pole of the system with frequency of 0.03 Hz and damping ratio of 0.7 is selected. The controller response is evaluated by running a HAWC2 time-domain simulation with wind speed steps from cut-in to cut-out and checking the overshoot and settling time of the response (rotor speed, pitch, power) between the operating point transitions (Figure 41).

6.2 HAWC2 Definition of the Design Load Basis

For the evaluation of lifetime extreme and fatigue loads in the time domain, the wind turbine model is set up in HAWC2 [17]. The setup of the load cases for the DLB follows the DTU interpretation of the recommendations from the International Electrotechnical Commission [45, 46]. Only a subset of the full DLB is evaluated in order to best quantify the performance of the turbine in load cases that do not depend on faults and specific controller tuning. This comprises normal power production and extreme turbulence load cases as well as a time-domain evaluation of the power curve (with no wind shear and turbulence, here named DLC 1.0) (see Table 20). Yaw misalignment cases of $\pm 8°$ are considered, with six turbulence seeds per wind speed and direction, but no wind-wave misalignment. The load cases are defined for the specified site conditions shown in Table 21. The simulations of the total of 851 load cases are run in the DTU Wind Energy department cluster, and the results are postprocessed in terms of statistics using the methods described in Pedersen [47]. The characteristic loads applied to the blade sections for the strength analysis in Section 2.3, are computed as six component contemporaneous loads with load case group averaging and presented for the root section in Appendix A.

Table 20: Summary of design load cases. Legend: NTM - Normal Turbulence Model, ETM - Extreme Turbulence Model.

| Name	Case	PSF	Description	Wind Speed	Wind Dir.	Turb	Seeds	Shear
DLC 1.0	-	1.0	Power curve	3:1:25	0	-	1	-
DLC 1.2	F	1.0	Normal power production	3:1:25	−8/0/8	NTM	6	0.14
DLC 1.3	U	1.35	Extreme turbulence	3:1:25	−8/0/8	ETM	6	0.14
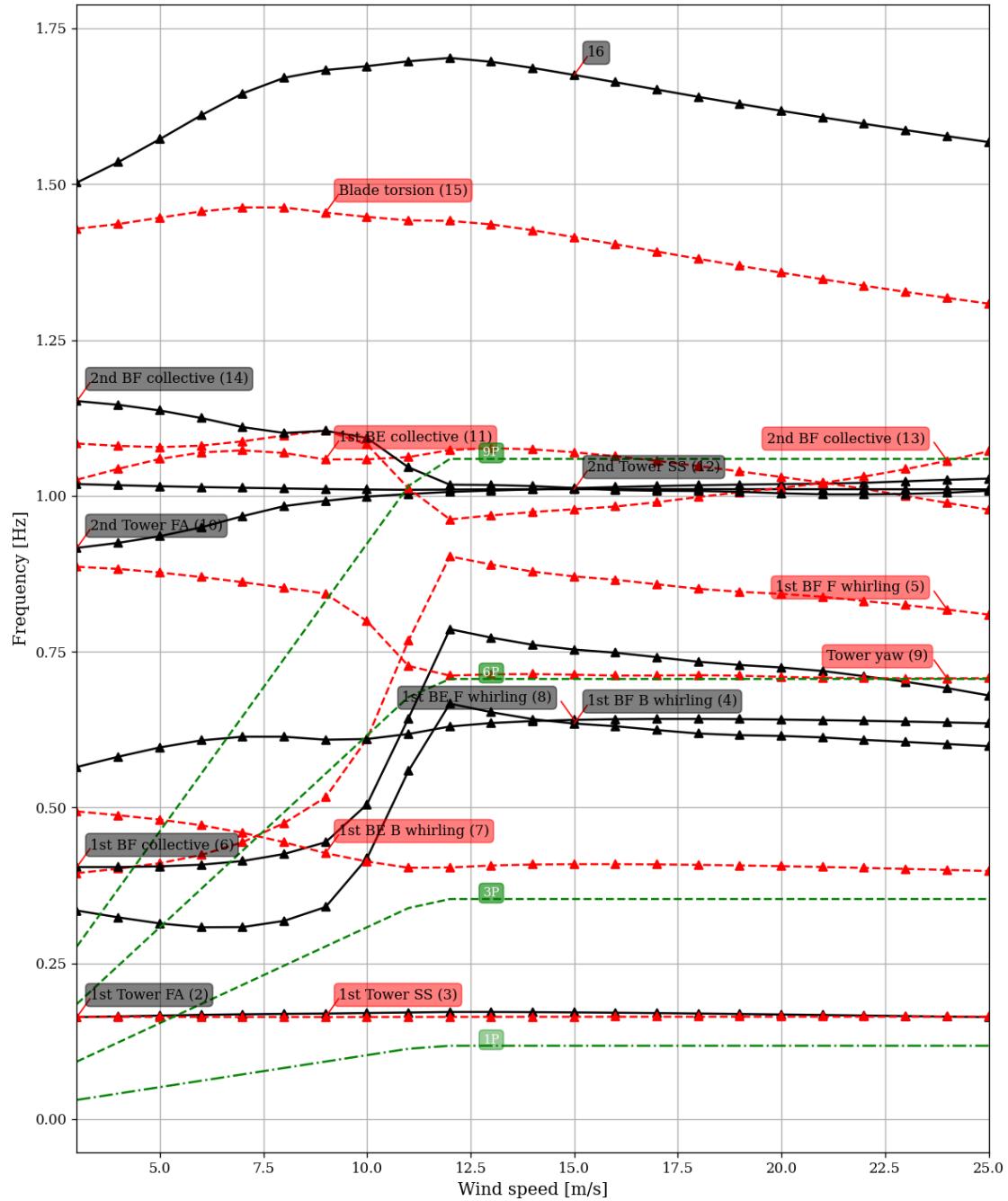
Figure 38: Full system frequencies in HAWCStab2. BF: blade flapwise, BE: blade edgewise, SS: side-side, FA: fore-aft. B: backward, F: forward. Numbers in parentheses indicate mode index where lowest number corresponds to lowest frequency.

Table 21: Summary of main parameters of site conditions. Legend: Vref - reference wind speed, TIref - reference turbulence intensity, k - shape parameter, λ - scale parameter, α - wind shear exponent, HS10 - significant wave height at $10\,\mathrm{m\,s^{-1}}$, TP10 - peak spectral period at $10\,\mathrm{m\,s^{-1}}$, WD - Water depth.

| Vref [$\mathrm{m\,s^{-1}}$]	TIref [-]	k [-]	λ [$\mathrm{m\,s^{-1}}$]	α [-]	HS10 [m]	TP10 [s]	WD [m]
50	0.14	2.0	10.0	0.14	1.53	7.65	34
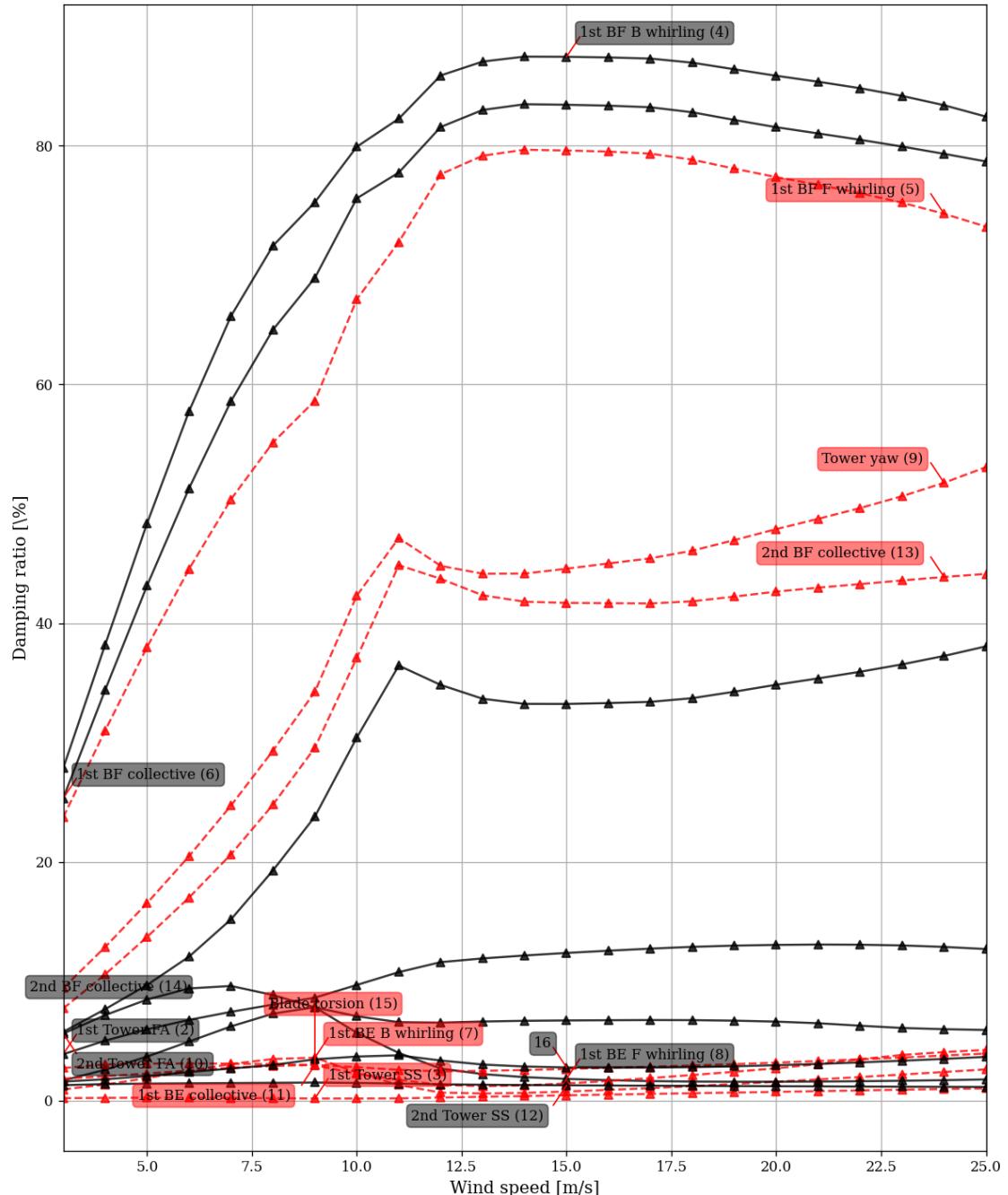
Figure 39: Full system damping in HAWCStab2. BF: blade flapwise, BE: blade edgewise, SS: side-side, FA: fore-aft. B: backward, F: forward. Numbers in parentheses indicate mode index where lowest number corresponds to lowest frequency.
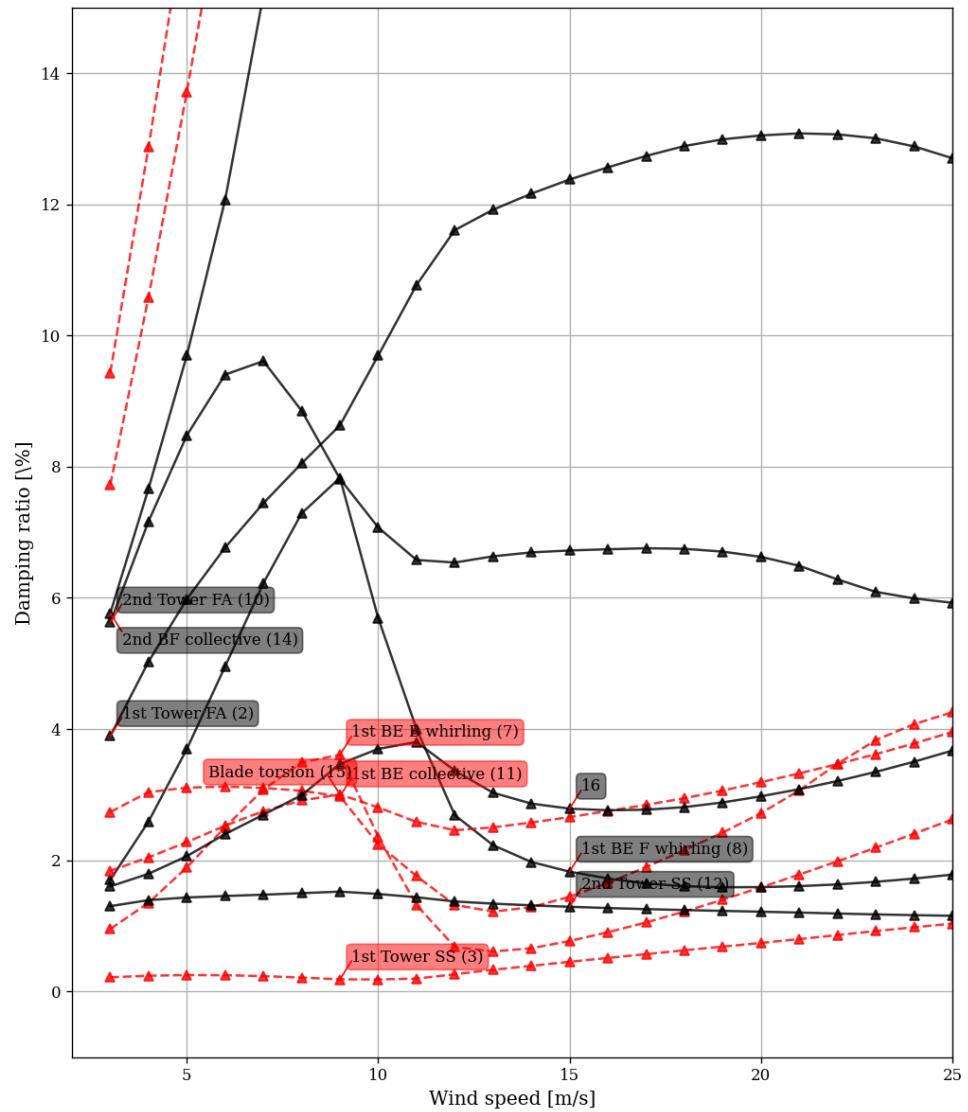
Figure 40: Full system damping in HAWCStab2, partial view from 0 to 15% damping ratio. BF: blade flapwise, BE: blade edgewise, SS: side-side, FA: fore-aft. B: backward, F: forward. Numbers in parentheses indicate mode index where lowest number corresponds to lowest frequency.
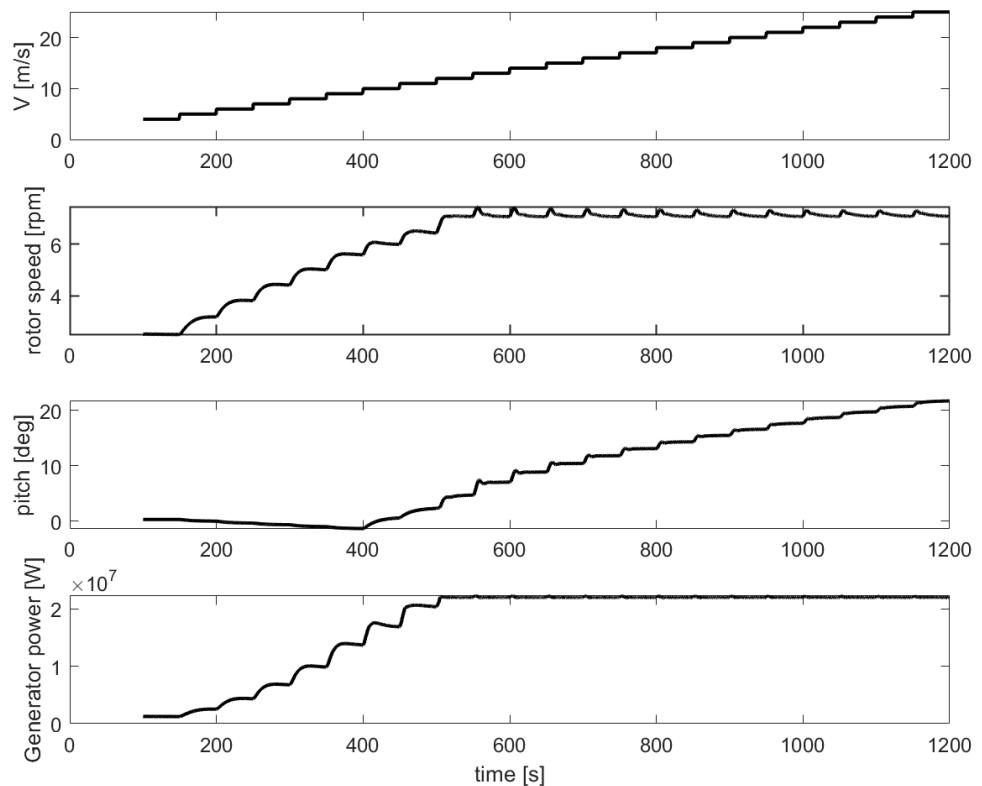
Figure 41: Time response in wind steps from cut-in to cut-out in HAWC2 (top to bottom: wind speed, rotor speed, pitch, generator power).

6.3   Results of the Design Load Basis – Fixed Bottom

The absolute min/max extreme loads for the main components are summarized in Table 22, together with the specific load case where they occur. The lifetime fatigue loads for the main components are summarized in Table 23. The HAWC2 coordinate systems are used.

Table 22: Summary of extreme loads and associated load cases for the fixed-bottom configuration (units: kN m for moments, m for deflection; SB: monopile base, TB: tower base, TT: tower top, MB: main bearing, BR: blade root, BTDy: blade tip flapwise deflection).

Name	Min Incl. PSF	Max Incl. PSF	DLC Min	DLC Max
MxSB	-1.04E+06	1.21E+06	13-wsp03-wdir008-s18001	13-wsp04-wdir000-s5002
MySB	-8.60E+05	9.17E+05	13-wsp03-wdir000-s4001	13-wsp03-wdir000-s4001
MzSB	-1.37E+05	1.40E+05	13-wsp25-wdir008-s17023	13-wsp14-wdir352-s11012
MxTB	-7.60E+05	8.35E+05	13-wsp03-wdir008-s18001	13-wsp04-wdir000-s5002
MyTB	-6.09E+05	6.49E+05	13-wsp03-wdir000-s4001	13-wsp03-wdir000-s4001
MzTB	-1.36E+05	1.40E+05	13-wsp25-wdir008-s17023	13-wsp14-wdir352-s11012
MxTT	-2.47E+05	1.51E+04	13-wsp23-wdir352-s8021	13-wsp22-wdir008-s16020
MyTT	-1.20E+04	6.13E+04	13-wsp03-wdir000-s4001	13-wsp19-wdir352-s9017
MzTT	-1.36E+05	1.39E+05	13-wsp25-wdir008-s17023	13-wsp14-wdir352-s11012
MxMB	-1.40E+05	1.43E+05	13-wsp06-wdir008-s14004	13-wsp22-wdir000-s6020
MyMB	-1.50E+05	1.39E+05	13-wsp06-wdir008-s14004	13-wsp25-wdir000-s3023
MzMB	-5.21E+04	0.00E+00	13-wsp25-wdir008-s14023	13-wsp04-wdir352-s8002
MxBR	-1.93E+05	8.14E+04	13-wsp09-wdir000-s4007	13-wsp25-wdir008-s14023
MyBR	-8.18E+04	8.24E+04	13-wsp22-wdir000-s4020	13-wsp09-wdir000-s1007
MzBR	-1.68E+03	1.96E+03	13-wsp22-wdir000-s5020	13-wsp11-wdir008-s14009
BTDy	-2.34E+01	4.47E+01	13-wsp25-wdir008-s14023	13-wsp09-wdir000-s4007

Few interesting component loads are shown here in detail. For the support structure bottom fore-aft moment, the mean/max/min values are shown in Figure 42, with the top 10 min/max values and associated load cases in Figure 43. For the tower bottom fore-aft moment, the mean/max/min values are shown in Figure 44, with the top 10 min/max values and associated load cases in Figure 45. For the blade root flapwise moment, the mean/max/min values are shown in Figure 46, with the top 10 min/max values and associated load cases in Figure 47.

The mean/min/max values (averaged per wind speed bin) of the blade root flapwise moment from the DLB evaluation are compared to the steady-state values from HAWCStab2 in Figure 48. The min/max values (averaged per wind speed bin) of the flapwise and edgewise moments distributed along the blade span are shown in in Figure 49. The mean/max values (averaged per wind speed bin) of the blade tip flapwise deflection from the DLB evaluation are compared to the steady-state values from HAWCStab2 in Figure 50. With a static tower clearance of approximately 41 m, there is insufficient tower clearance if PSFs are considered. The max values are presented from both DLC 1.2 and DLC 1.3 because in a realistic operation at high turbulence, increased peak shaving would be applied, limiting the loads and deflection to levels closer to those observed for DLC 1.2. It remains the goal of future work to implement this control strategy. The power curves from the DLB evaluation are also compared to the steady-state power curve from HAWCStab2 in Figure 51. The comparison of resulting AEP for the site conditions is shown in Table 24.

Table 23: Summary of lifetime fatigue loads for the fixed-bottom configuration (25 years, units: kN m, SB: monopile base, TB: tower base, TT: tower top, MB: main bearing, BR: blade root, m: Wöhler slope, Neq: lifetime equivalent load numbe).

Name	Lifetime Equivalent Load	m	Neq
MxSB	3.804E+05	4	1E+07
MySB	3.273E+05	4	1E+07
MzSB	6.512E+04	4	1E+07
MxTB	2.272E+05	4	1E+07
MyTB	2.144E+05	4	1E+07
MzTB	6.492E+04	4	1E+07
MxTT	6.905E+04	4	1E+07
MyTT	1.119E+04	4	1E+07
MzTT	6.391E+04	4	1E+07
MxMB	1.023E+05	4	1E+07
MyMB	1.023E+05	4	1E+07
MzMB	5.638E+03	4	1E+07
MxBR	7.259E+04	10	1E+07
MyBR	8.023E+04	10	1E+07
MzBR	1.230E+03	10	1E+07
PitchBearing	3.755E+21	3	1E+00
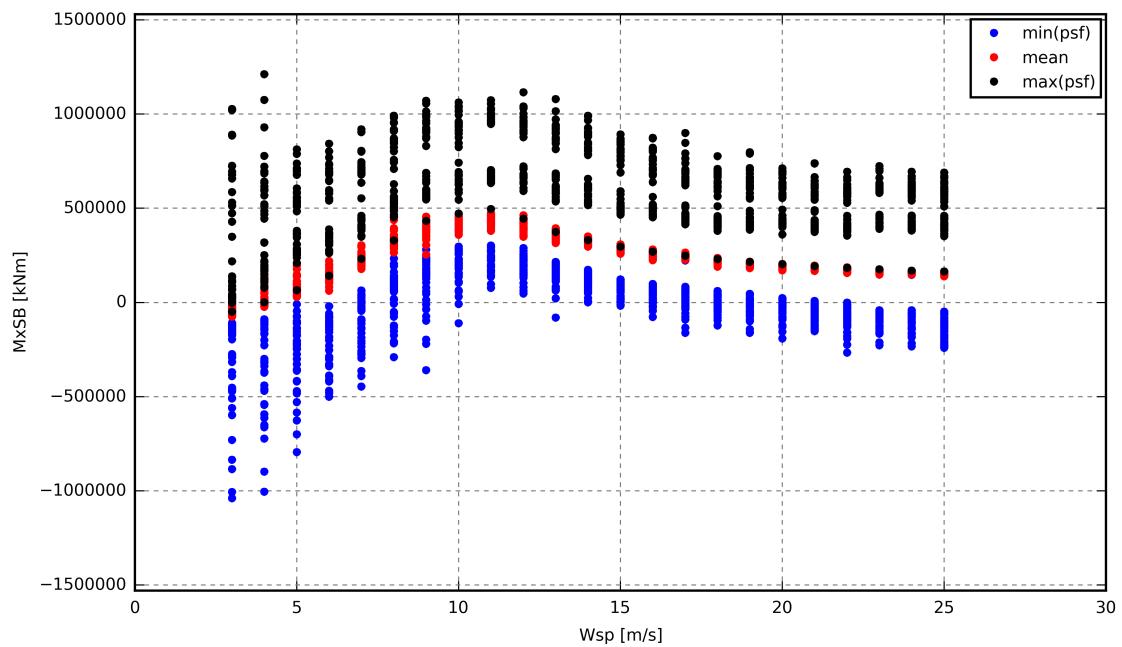
Figure 42: Load statistics for support structure bottom fore-aft moment.
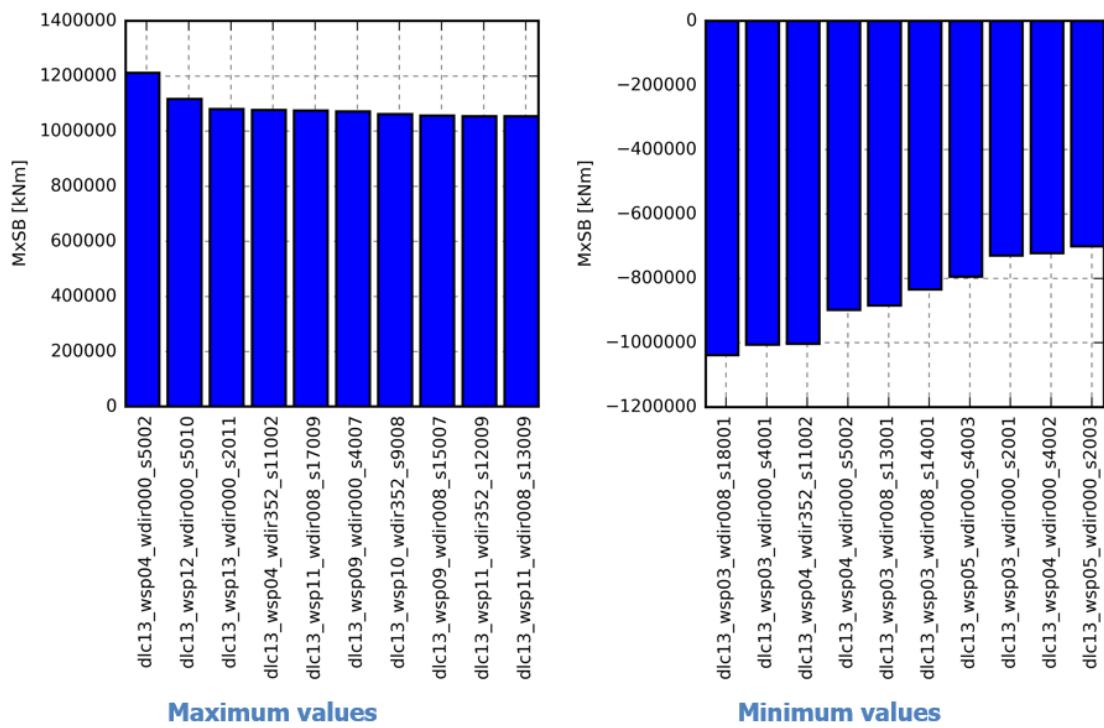
Figure 43: Load cases for extreme support structure bottom fore-aft moment.
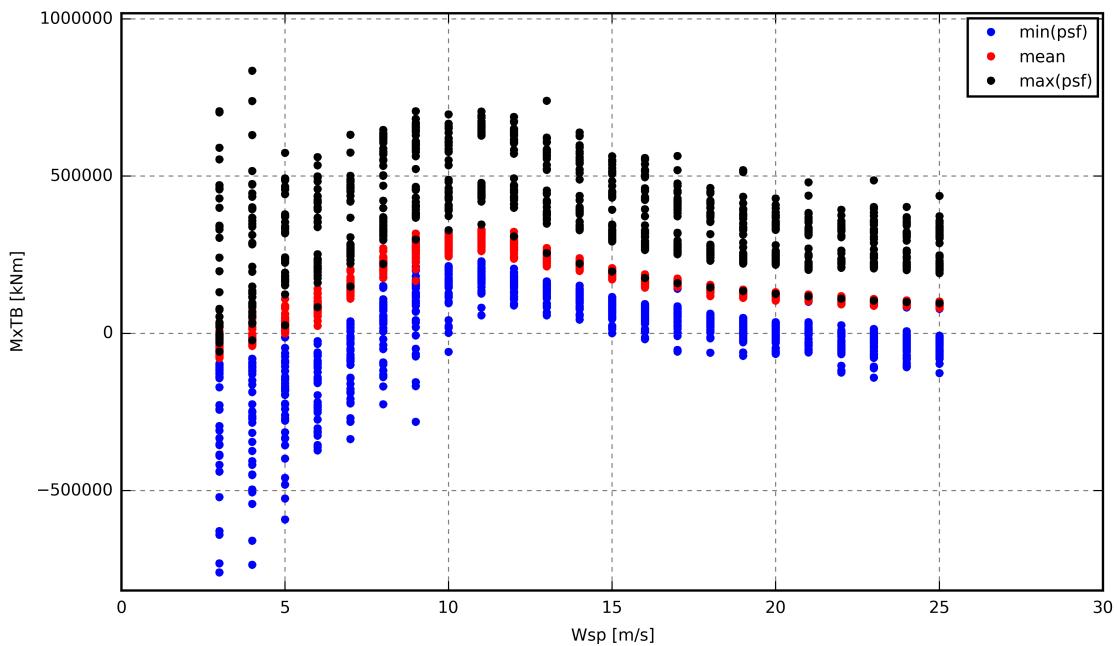
Figure 44: Load statistics for tower bottom fore-aft moment.
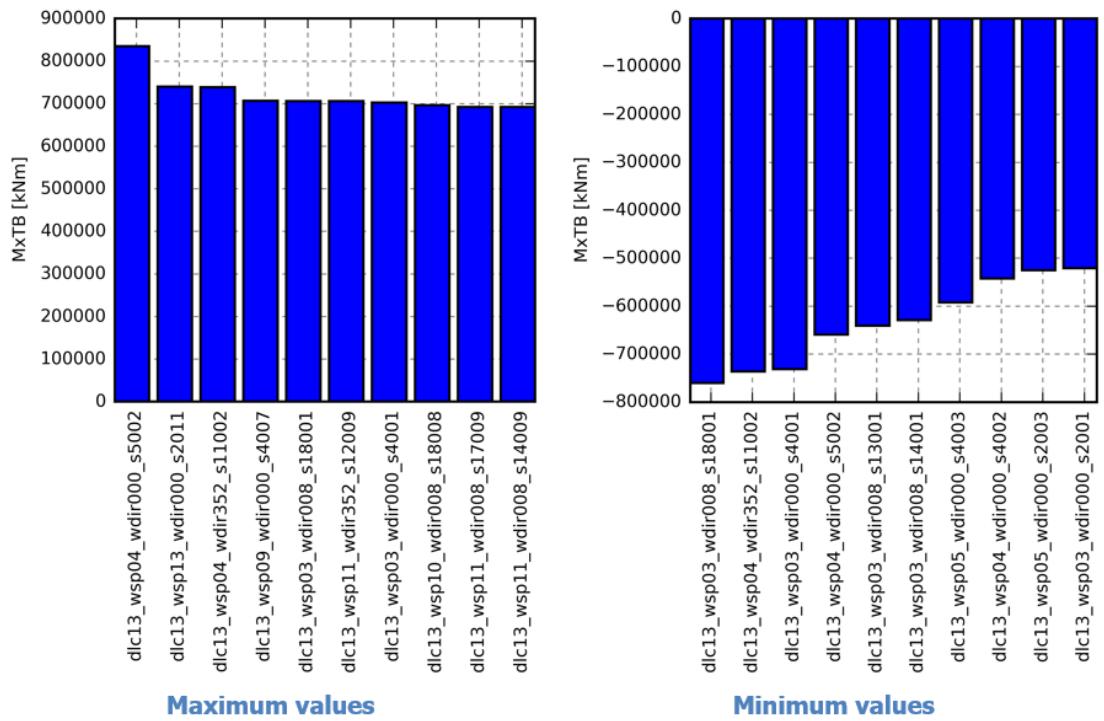
Figure 45: Load cases for extreme tower bottom fore-aft moment.
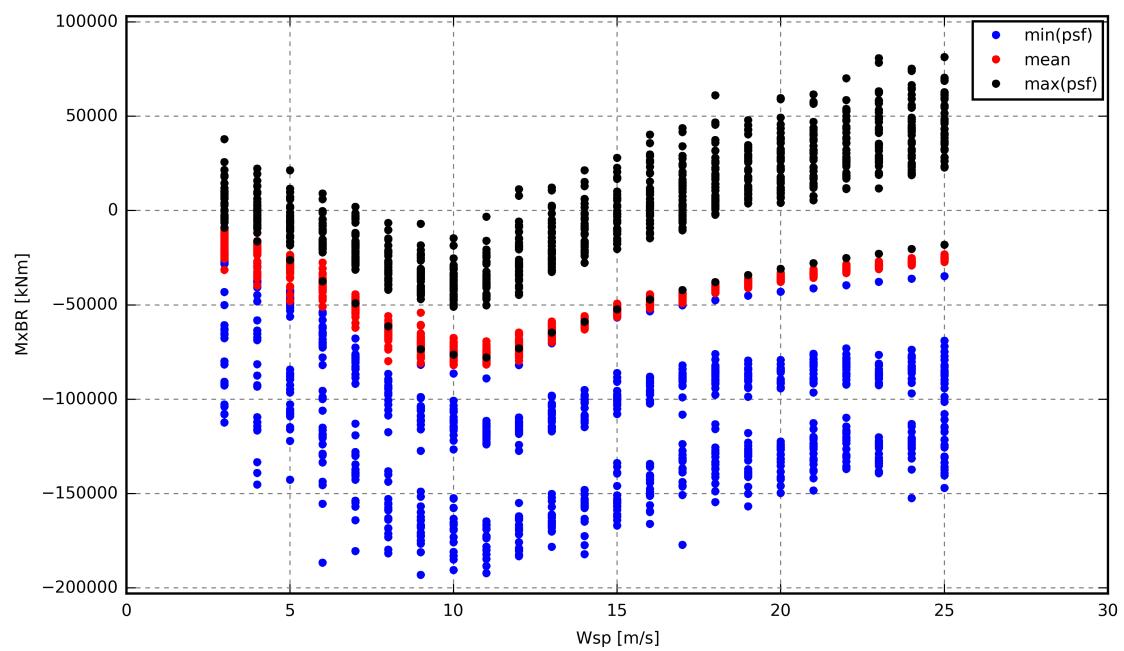

Figure 46: Load statistics for blade root flapwise moment.
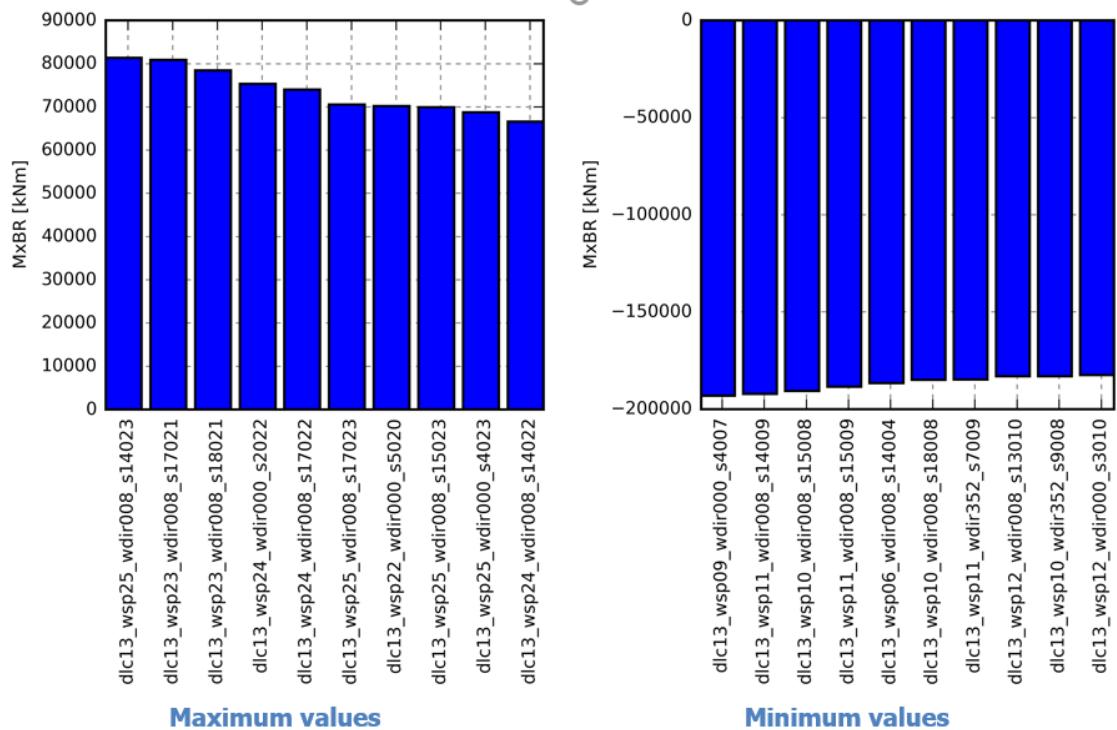
Figure 47: Load cases for extreme blade root flapwise moment.
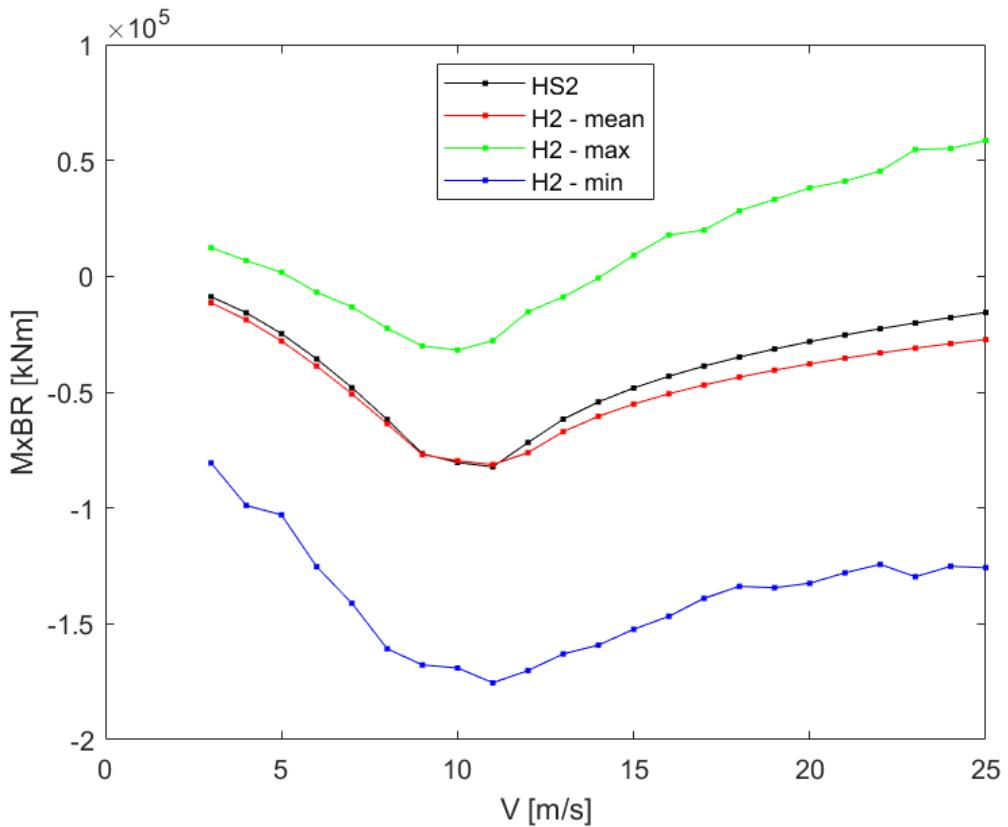
Figure 48: Comparison of blade root flapwise moment average statistics between HAWC2 DLB and HAWCStab2.
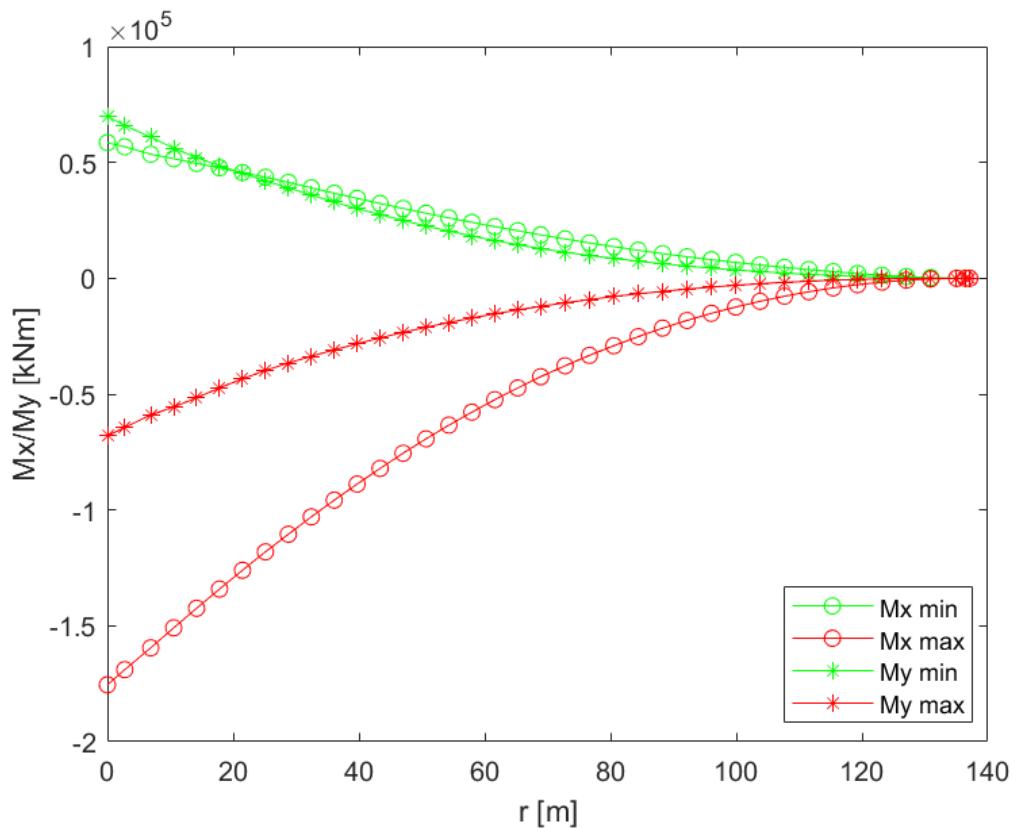
Figure 49: Distribution of Mx/My moment extremes along blade span.

Table 24: Summary of AEP from steady-state HAWCStab2 and time-domain HAWC2 simulations and comparison to steady-state AEP

| Case	AEP [W h]	% AEP [-]
HAWCStab2 steady-state	1.1859e+11	-
HAWC2 - DLC 1.0	1.1307e+11	-4.6
HAWC2 - DLC 1.2	1.1337e+11	-4.4
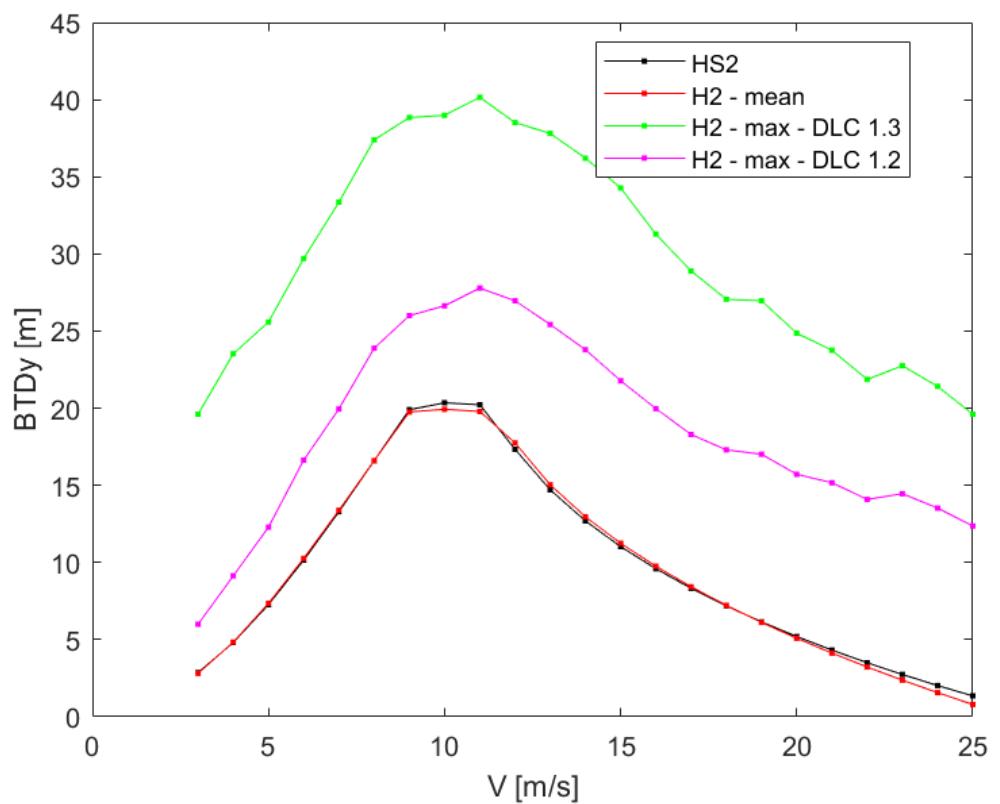
Figure 50: Comparison of blade tip flapwise deflection average statistics between HAWC2 DLB and HAWCStab2.
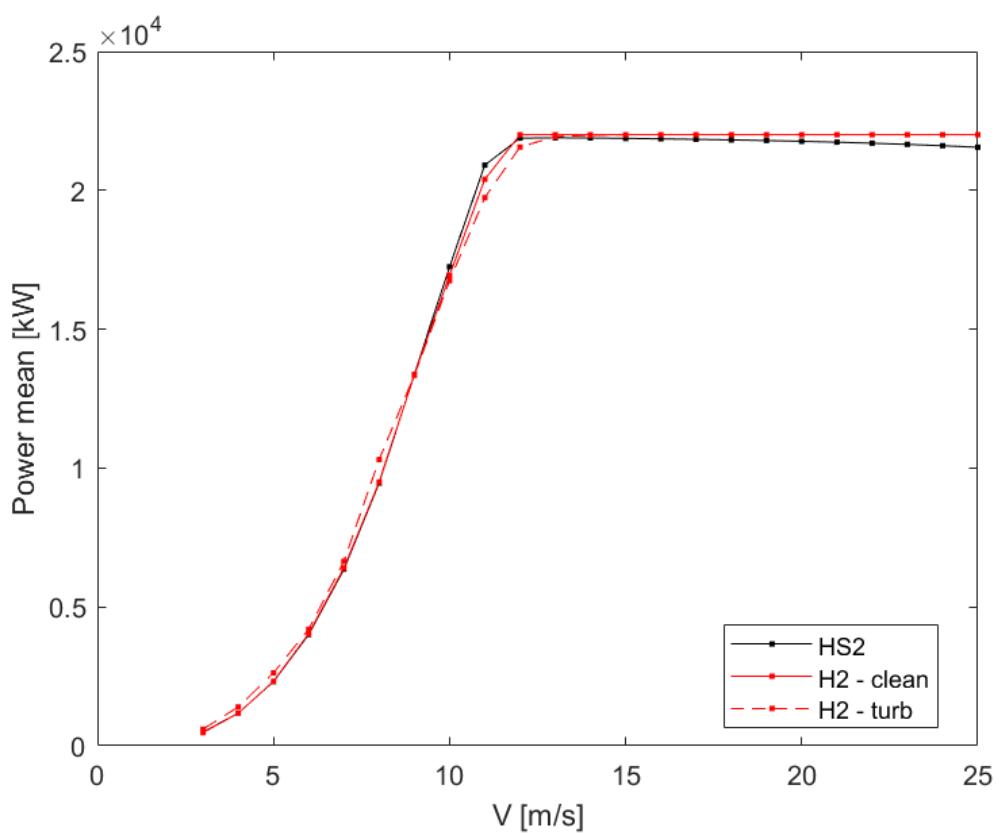
Figure 51: Comparison of power average statistics between HAWC2 DLB and HAWCStab2 (HS2: steady-state values, H2-clean: average binned values from DLC 1.0, H2-turb: average binned values from DLC 1.2).

6.4 Results of the Design Load Basis – Floating

The absolute min/max extreme loads estimated by HAWC2 for the main components are summarized in Table 25, together with the specific load case where they occur. The lifetime fatigue loads for the main components are summarized in Table 26.

Table 25: Summary of extreme loads and associated load cases for the floating configuration (units: kN m for moments, m for deflection, SB: monopile base, TB: tower base, TT: tower top, MB: main bearing, BR: blade root, BTDy: blade tip flapwise deflection)

Name	Min Incl. PSF	Max Incl. PSF	DLC Min	DLC Max
MxTB	−1.10E+06	1.46E+06	13-wsp22-wdir000-s4020	13-wsp22-wdir000-s4020
MyTB	−5.09E+05	7.37E+05	13-wsp22-wdir008-s15020	13-wsp20-wdir008-s17018
MzTB	−1.44E+05	1.50E+05	13-wsp23-wdir008-s18021	13-wsp23-wdir352-s8021
MxTT	−2.48E+05	2.56E+04	13-wsp23-wdir352-s8021	13-wsp25-wdir000-s3023
MyTT	−2.75E+04	7.76E+04	13-wsp22-wdir000-s4020	13-wsp22-wdir352-s9020
MzTT	−1.43E+05	1.49E+05	13-wsp23-wdir008-s18021	13-wsp23-wdir352-s8021
MxMB	−1.43E+05	1.48E+05	13-wsp23-wdir352-s9021	13-wsp25-wdir008-s17023
MyMB	−1.39E+05	1.34E+05	13-wsp23-wdir008-s18021	13-wsp21-wdir008-s18019
MzMB	−6.57E+04	3.59E+04	13-wsp22-wdir000-s4020	13-wsp22-wdir000-s4020
MxBR	−2.17E+05	1.02E+05	13-wsp22-wdir000-s4020	13-wsp24-wdir008-s17022
MyBR	−1.00E+05	9.65E+04	13-wsp12-wdir000-s3010	13-wsp09-wdir352-s12007
MzBR	−2.10E+03	3.04E+03	13-wsp25-wdir008-s16023	13-wsp22-wdir000-s4020
BTDy	−2.51E+01	4.42E+01	13-wsp24-wdir008-s17022	13-wsp11-wdir008-s16009

Table 26: Summary of lifetime fatigue loads for the floating configuration (25 years, units: kN m, SB: monopile base, TB: tower base, TT: tower top, MB: main bearing, BR: blade root, m: Wöhler slope, Neq: lifetime equivalent load number)

Name	Lifetime Equivalent Load	m	Neq
MxTB	5.054E+05	4	1E+07
MyTB	3.566E+05	4	1E+07
MzTB	6.639E+04	4	1E+07
MxTT	6.973E+04	4	1E+07
MyTT	1.674E+04	4	1E+07
MzTT	6.570E+04	4	1E+07
MxMB	9.889E+04	4	1E+07
MyMB	9.888E+04	4	1E+07
MzMB	1.221E+04	4	1E+07
MxBR	8.145E+04	10	1E+07
MyBR	8.371E+04	10	1E+07
MzBR	1.281E+03	10	1E+07
PitchBearing	1.069E+22	3	1E+00

7 Conclusion and Outlook

This report documents the design basis, detailed properties and performance of the IEA 22 MW RWT released as a result of a joint international effort coordinated in the IEA Wind TCP Task 55.

The IEA 22 MW RWT offers a well-defined, common and open source platform to investigate technology challenges and innovations for the next generation of offshore wind turbines to be deployed in the latter half of the 2020s. The turbine allows the research community to conduct detailed aeroelastic predictions using popular numerical models, and investigate possible inconsistencies between these. An initial study comparing predictions among HAWC2/HAWCStab2, OpenFAST, DNVGL's Bladed, and QBlade from the Technical University of Berlin in Germany can be found in Collier et al. [48]. The study concludes that the agreement between the four codes is generally satisfactory, although differences are observed. The discrepancies suggest that thorough verification and validation studies should be conducted, as modern aeroelastic tools struggle to agree with their predictions on the dynamic behavior of the next generation of offshore wind turbines.

The modelling fidelity presented in this report has been limited to address medium-fidelity aeroelastic tools, however, the IEA 22 MW RWT is also suitable for high-fidelity modelling, such as computational fluid dynamics (CFD) and computational structural modelling (CSD). Zahle et al. [49] presents a study on aeroelastic steady-state modelling based on low- and medium-fidelity aerodynamic modelling compared to high-fidelity 3D CFD coupled to a nonlinear beam solver, showing good agreement across the fidelities. The numerical model developed for this study will be made publicly available.

Further details of the design, including a WindIO definition of the turbine, as well as OpenFAST, HAWC2, QBlade and WISDEM input files, are available at the IEA Wind Task 37 GitHub page, see `https://github.com/IEAWindTask37/IEA-22-280-RWT`, where also possible updates to the design will be published.

Acknowledgments

References

[1] G. Bywaters, V. John, J. Lynch, P. Mattila, G. Norton, J. Stowell, M. Salata, O. Labath, A. Chertok, and D. Hablanian, "Northern power systems windpact drive train alternative design study report; period of performance: April 12, 2001 to january 31, 2005," 10 2004. [Online]. Available: https://www.osti.gov/biblio/15007774

[2] J. Jonkman, S. Butterfield, W. Musial, and G. Scott, "Definition of a 5-mw reference wind turbine for offshore system development," 2 2009. [Online]. Available: https://www.osti.gov/biblio/947422

[3] C. Bak, F. Zahle, R. Bitsche, T. Kim, A. Yde, L. C. Henriksen, P. B. Andersen, A. Natarajan, and M. Hansen, "Design and performance of a 10 MW wind turbine," To be submitted, Jul. 2013.

[4] "Iea wind task 37," Last accessed: 10/1/2024. [Online]. Available: https://iea-wind.org/task37

[5] P. Bortolotti, H. Tarrés, K. Dykes, K. Merz, L. Sethuraman, D. Verelst, and F. Zahle, IEA Wind TCP Task 37: Systems Engineering in Wind Energy-WP2.1 Reference Wind Turbines. National Renewable Energy Laboratory (NREL), 2019.

[6] E. Gaertner, J. Rinker, L. Sethuraman, F. Zahle, B. Anderson, G. Barter, N. Abbas, F. Meng, P. Bortolotti, W. Skrzypinski, G. Scott, R. Feil, H. Bredmose, K. Dykes, M. Sheilds, C. Allen, and A. Viselli, "Definition of the IEA 15-megawatt offshore reference wind turbine," NREL/TP-75698, International Energy Agency, Tech. Rep., 2020. [Online]. Available: https://www.nrel.gov/docs/fy20osti/75698.pdf

[7] P. Bortolotti, C. Bay, G. Barter, E. Gaertner, K. Dykes, M. McWilliam, M. Friis-Moller, M. Molgaard Pedersen, and F. Zahle, "System modeling frameworks for wind turbines and plants: Review and requirements specifications," 5 2022.

[8] P. Veers, K. Dykes, R. Baranowski, C. Bay, P. Bortolotti, P. Doubrawa, S. MacDonald, S. Rooney, C. L. Bottasso, P. Fleming, S. E. Haupt, A. Hale, C. Hein, and A. Robertson, "Grand challenges revisited: Wind energy research needs for a global energy transition."

[9] "Iea wind task 55," Last accessed: 10/1/2024. [Online]. Available: https://iea-wind.org/task-55

[10] F. Zahle, K. Lønbæk, A. Li, and R. Riva, AESOpt - Aero-Structural Optimization Framework for Wind Turbine Design, 2023, version 0.32. [Online]. Available: https://aesopt.pages.windenergy.dtu.dk/aesopt

[11] K. Loenbaek, C. Bak, and M. McWilliam, "A method for preliminary rotor design – part 2: Wind turbine optimization with radial independence," Wind Energy Science, vol. 6, no. 3, pp. 917–933, 2021. [Online]. Available: https://wes.copernicus.org/articles/6/917/2021/

[12] J. P. Blasques and M. Stolpe, "Multi-material topology optimization of laminated composite beam cross sections," Composite Structures, vol. 94, no. 11, pp. 3278 – 3289, 2012.

[13] "http://becas.dtu.dk/."

[14] A. Li, M. Gaunaa, G. Pirrung, and S. Horcas, "A computationally efficient engineering aerodynamic model for non-planar wind turbine rotors," Wind Energy Science, vol. 7, pp. 75–104, 2022.

[15] A. Li, G. Pirrung, M. Gaunaa, H. Madsen, and S. Horcas, "A computationally efficient engineering aerodynamic model for swept wind turbine blades," Wind Energy Science, vol. 7, pp. 129–160, 2022.

[16] A. Li, M. Gaunaa, G. Pirrung, A. Meyer Forsting, and S. Horcas, "How should the lift and drag forces be calculated from 2-d airfoil data for dihedral or coned wind turbine blades?" Wind Energy Science, vol. 7, no. 4, pp. 1341–1365, 2022.

[17] T. Larsen and A. Hansen, "How 2 hawc2, the user's manual," Risø National Laboratory, Tech. Rep. 1597(ver. 3-1)(EN), 2007.

[18] P. Fuglsang and K. Thomsen, "Site-specific design optimization of 1.5-2.0 mw wind turbines," Journal of Solar Energy Engineering, vol. 123, pp. 296–303, 2001.

[19] J. S. Gray, J. T. Hwang, J. R. R. A. Martins, K. T. Moore, and B. A. Naylor, "OpenMDAO: An open-source framework for multidisciplinary design, analysis, and optimization," Structural and Multidisciplinary Optimization, vol. 59, no. 4, pp. 1075–1104, April 2019.

[20] A. Wächter and L. T. Biegler, "On the implementation of a primal-dual interior point filter line search algorithm for large-scale nonlinear programming," Mathematical Programming, vol. 106, no. 1, pp. 25–57, 2006.

[21] "http://pyopt.org/."

[22] E. Camarena, E. Anderson, J. Paquette, P. Bortolotti, R. Feil, and N. Johnson, "Land-based wind turbines with flexible rail-transportable blades – part 2: 3d finite element design optimization of the rotor blades," Wind Energy Science, vol. 7, no. 1, pp. 19–35, 2022. [Online]. Available: https://wes.copernicus.org/articles/7/19/2022/

[23] J. A. Michelsen, "Block structured multigrid solution of 2D and 3D elliptic PDEs," Technical University of Denmark, Tech. Rep. AFM 94-06, 1994.

[24] N. N. Sørensen, "General purpose flow solver applied to flow over hills," Risoe National Laboratory, Tech. Rep. Risø-R-827(EN), 1995.

[25] ——, "HypGrid2D—a 2-D mesh generator," Risoe National Laboratory, Tech. Rep. Risø-R-1035(EN), 1998.

[26] "https://github.com/wisdem/airfoilpreppy," 2022.

[27] Z. Du and M. Selig, A 3-D stall-delay model for horizontal axis wind turbine performance prediction.

[28] M. Hansen, "Aeroelastic stability analysis of wind turbines using an eigenvalue approach," Wind Energy, vol. 7, no. 2, pp. 133–143, 2004, 2003 European Wind Energy Conference and Exhibition, EWEC 2003 ; Conference date: 16-06-2003 Through 19-06-2003.

[29] J. N. Stander, G. Venter, and M. J. Kamper, "Review of direct-drive radial flux wind turbine generator mechanical design," Wind Energy, vol. 15, no. 3, pp. 459–472, 2012.

[30] G. E. Barter, L. Sethuraman, P. Bortolotti, J. Keller, and D. A. Torrey, "Beyond 15 mw: A cost of energy perspective on the next generation of drivetrain technologies for offshore wind turbines," Applied Energy, vol. 344, p. 121272, 2023.

[31] L. Sethuraman, G. Barter, P. Bortolotti, J. Keller, and D. A. Torrey, "Optimization and comparison of modern offshore wind turbine generators using generatorse 2.0," in 2023 IEEE International Electric Machines & Drives Conference (IEMDC), 2023, pp. 1–7.

[32] D. Meeker. Finite element method magnetics (femm) v4.2. Accessed: 2023-12-06. [Online]. Available: www.femm.info

[33] Altair® flux® applications. Accessed: 2023-04-17. [Online]. Available: https://www.altair.com/flux-applications/

[34] Altair Hyperstudy Applicaions. Accessed: 2023-04-17. [Online]. Available: https://www.altair.com/hyperstudy-applications

[35] E. B. Smith, "Design av nacelle for en 10 mw vindturbin," Master's thesis, Institutt for produktutvikling og materialer, 2012.

[36] C. Allen, A. Viselli, H. Dagher, A. Goupee, E. Gaertner, N. Abbas, M. Hall, and G. Barter, "Definition of the UMaine VolturnUS-S reference platform developed for the IEA Wind 15-megawatt offshore reference wind turbine," NREL/TP-76773, International Energy Agency, Tech. Rep.

[37] M. Hall, S. Housner, D. Ogden, D. Zalkind, G. Barter, and P. Bortolotti, "RAFT (Response Amplitudes of Floating Turbines)," US National Renewewable Energy Laboratory, Tech. Rep., 2022.

[38] International Electrotechnical Commission, "Wind energy generation systems - part 3-1: Design requirements for fixed offshore wind turbines," Tech. Rep. 61400-3-1, 2018.

[39] ——, "Wind energy generation systems - part 3-2: Design requirements for floating offshore wind turbines," Tech. Rep. 61400-3-2, 2019.

[40] C.-H. Lee, "Wamit theory manual," Massachusettes Institute of Technology, Cambridge, MA, Tech. Rep. 95-2, October 1995. [Online]. Available: https://www.wamit.com/Publications/tmanual.pdf

[41] J. M. Jonkman, A. N. Robertson, and G. J. Hayman, "HydroDyn user's guide and theory manual (draft)," National Renewable Energy Laboratory, Golden, CO, Tech. Rep., 2014. [Online]. Available: https://www.nrel.gov/wind/nwtc/assets/downloads/HydroDyn/HydroDyn_Manual.pdf

[42] O. M. Faltinsen, Sea loads on ships and offshore structures.   Cambridge University Press, 1990.

[43] M. Hall, S. Housner, S. Sirnivas, and S. Wilson, "MoorPy: Quasi-static mooring analysis in Python," National Renewable Energy Laboratory, Golden, CO, 2021. [Online]. Available: https://doi.org/10.11578/dc.20210726.1

[44] M. Hansen and L. Henriksen, Basic DTU Wind Energy controller, ser. DTU Wind Energy E.   Denmark: DTU Wind Energy, 2013, no. 0028, contract Number: EUDP project Light Rotor; Project Number 46-43028-Xwp3 The report number is DTU-Wind-Energy-Report-E-0028 and not DTU-Wind-Energy-Report-E-0018 as stated inside the report.

[45] A. Natarajan, M. Hansen, and S. Wang, "Design load basis for offshore wind turbines: Dtu wind energy report no. e-0133," DTU Wind Energy, Tech. Rep., 2016.

[46] M. Hansen, K. Thomsen, A. Natarajan, and A. Barlas, "Design load basis for onshore turbines - revision 00," DTU Wind Energy, Denmark, Tech. Rep. 0074(EN), 2015.

[47] M. Pedersen, "Post processing of design load cases using pdap," DTU Wind Energy, Denmark, Tech. Rep. 0371, 2014.

[48] W. Collier, O. Dilek, T. Barlas, F. Zahle, P. Bortolotti, D. Marten, C. Jensen, E. Branlard, D. Zalkind, and K. Lønbæk, "Aeroelastic code comparison using the iea 22mw reference turbine," TORQUE 2024 - To appear.

[49] F. Zahle, A. Li, K. Lønbæk, N. N. Sørensen, and R. Riva, "Multi-fidelity, steady-state aeroelastic modelling of a 22-megawatt wind turbine," TORQUE 2024 - To appear.

Appendix A   Design Loads

This appendix describes the format of the blade design loads computed using HAWC2, described in Section 6. Results are presented in Table 27. The characteristic loads applied to the blade sections for the strength analysis in Section 2.3, are computed as six component contemporaneous loads with load case group averaging. The extreme values (maxima and minima) of the corresponding load components are located at the diagonal. In addition to the extreme values of the load components the maximum magnitude of the resulting transverse force F_{res} and the maximum magnitude of the resulting bending moment M_{res} are listed. The simultaneous loads of the other load components are given in the columns. The values given do not include the safety factor for the loads, and since they stem from DLC1.3 a safety factor of 1.35 should be applied. The forces and moments relate to the mid-chord reference line of the respective cross-section, and are given in a coordinate system aligned with the HAWC2 'c2def' reference.

Table 27: Table showing example of blade design loads, here shown for the root section.

Case	F_x [MN]	F_y [MN]	F_z [MN]	F_{res} [MN]	M_x [MNm]	M_y [MNm]	M_z [MNm]	M_{res} [MNm]
F_x max	1.143	1.164	1.874	1.652	-46.843	45.539	-0.033	67.964
F_x min	-1.049	0.359	1.812	1.127	-25.646	-47.140	-0.316	54.947
F_y max	0.087	1.777	1.777	1.861	-123.156	9.918	0.515	125.393
F_y min	-0.495	-0.463	2.133	0.721	35.430	-15.076	-0.172	40.578
F_z max	0.078	0.620	3.056	0.654	-14.739	4.099	-0.017	18.255
F_z min	0.031	0.050	-0.636	0.108	-4.446	1.669	0.002	8.097
F_{res} max	0.949	1.738	1.884	1.986	-77.422	35.465	-0.029	85.469
M_x max	-0.313	-0.408	2.374	0.615	39.097	-9.107	-0.074	42.793
M_x min	-0.203	1.723	1.271	1.797	-127.524	1.319	0.718	128.800
M_y max	1.109	1.378	1.325	1.771	-100.128	50.900	-0.498	112.467
M_y min	-0.997	0.337	1.806	1.075	-20.886	-48.426	-0.498	54.667
M_z max	-0.587	1.532	1.432	1.643	-115.250	-18.065	1.090	116.764
M_z min	-0.737	0.114	1.886	0.777	3.341	-36.414	-0.910	38.032
M_{res} max	0.316	1.724	1.202	1.854	-125.651	20.268	0.305	129.340

DTU Wind
Department of Wind and Energy Systems
Technical University of Denmark

Frederik Zahle
Risø Campus Building 118
Frederiksborgvej 399
DK-4000 Roskilde
frza@dtu.dk